

**A NOVEL ALGORITHM FOR DETECTING ISOLATED
GREEN FLUORESCENTLY-LABELED CELLS IN
CRYO-IMAGING DATA**

THANAPONG CHATBOONWARD

**MASTER OF ENGINEERING
IN BIOMEDICAL ENGINEERING**

ลิขสิทธิ์มหาวิทยาลัยเชียงใหม่
Copyright© by Chiang Mai University
All rights reserved

**GRADUATE SCHOOL
CHIANG MAI UNIVERSITY
MAY 2022**

**A NOVEL ALGORITHM FOR DETECTING ISOLATED
GREEN FLUORESCENTLY-LABELED CELLS IN
CRYO-IMAGING DATA**

THANAPONG CHATBOONWARD

**MASTER OF ENGINEERING
IN BIOMEDICAL ENGINEERING**

ลิขสิทธิ์มหาวิทยาลัยเชียงใหม่
Copyright© by Chiang Mai University
All rights reserved

**GRADUATE SCHOOL
CHIANG MAI UNIVERSITY
MAY 2022**

**A NOVEL ALGORITHM FOR DETECTING ISOLATED
GREEN FLUORESCENTLY-LABELED CELLS IN
CRYO-IMAGING DATA**

THANAPONG CHATBOONWARD

**A THESIS SUBMITTED TO CHIANG MAI UNIVERSITY IN PARTIAL
FULFILLMENT OF THE REQUIREMENTS FOR THE DEGREE OF
MASTER OF ENGINEERING
IN BIOMEDICAL ENGINEERING**

ลิขสิทธิ์มหาวิทยาลัยเชียงใหม่
Copyright© by Chiang Mai University
All rights reserved

GRADUATE SCHOOL, CHIANG MAI UNIVERSITY

MAY 2022


**A NOVEL ALGORITHM FOR DETECTING ISOLATED
GREEN FLUORESCENTLY-LABELED CELLS IN
CRYO-IMAGING DATA**


THANAPONG CHATBOONWARD


THIS THESIS HAS BEEN APPROVED TO BE A PARTIAL FULFILLMENT
OF THE REQUIREMENTS FOR THE DEGREE OF
MASTER OF ENGINEERING
IN BIOMEDICAL ENGINEERING

Examination Committee:

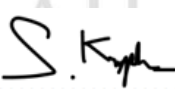
Advisor:


.....Chairman
(Prof.Dr. Kosin Chamnongthai)


.....
(Asst.Prof.Dr. Patiwet Wuttisarnwattana)


.....Member
(Asst.Prof.Dr. Patiwet Wuttisarnwattana)


.....Member
(Assoc.Prof.Dr. Nipon Theera-Umpon)


.....Member
(Assoc.Prof.Dr. Sarawut Kumphune)

12 May 2022

Copyright © by Chiang Mai University

ACKNOWLEDGEMENT

I would like to sincerely thanks to my thesis advisor, Assistant Professor Dr. Patiwet Wuttisarnwattana for his precious support and encouragement. I specially appreciate for his expert teaching and advice throughout the process of this challenging research. His patience and guidance for me made this difficult research possible. I would not have achieved this research without all the best support from him.

Finally, I would like to gratefully acknowledge my parents and my colleagues for their wonderful support throughout the entire course of my master's degree in biomedical engineering.

Thanapong Chatboonward



ลิขสิทธิ์มหาวิทยาลัยเชียงใหม่
Copyright© by Chiang Mai University
All rights reserved

หัวข้อปริญญานิพนธ์

ขั้นตอนวิธีใหม่สำหรับการตรวจหาเซลล์ที่ถูกแต่งด้วยสาร
ฟลูออเรสเซนต์สีเขียวที่มีลักษณะแยกโคคเคียวใน
ข้อมูลภาพโคร โออิมเมจ

ผู้เขียน

นายธนพงษ์ ฉัตรบุญวาสน์

ปริญญา

วิศวกรรมศาสตรมหาบัณฑิต (วิศวกรรมชีวการแพทย์)

อาจารย์ที่ปรึกษา

ผศ. ดร. ปฎิเวศ วุฒิสารวัฒนา

บทคัดย่อ

โคร โออิมเมจจึงเป็นเทคโนโลยีการสร้างภาพชีวการแพทย์สำหรับศึกษาการกระจายตัวของเซลล์ในร่างกายของสัตว์ทดลองขนาดเล็ก เทคโนโลยีนี้สามารถใช้เพื่อค้นหาเซลล์ที่สนใจได้ทุกที่ทั่วทั้งตัวของสัตว์ทดลองด้วยความแม่นยำในระดับเซลล์เดียว ในการศึกษาที่ผู้วิจัยสนใจในการตรวจหาที่เซลล์ที่ถูกย้อมด้วยสารฟลูออเรสเซนต์สีเขียวในตับของหนูทดลองที่มีภาวะ Graft-versus Host disease อย่างไรก็ตามการตรวจหาที่เซลล์มีความท้าทายสูงและยาก เนื่องจากอโต้ฟลูออเรสเซนต์ในตับโดยเฉพาะอย่างยิ่งที่เกิดจากท่อน้ำดีและถุงน้ำดี มีสเปกตรัมที่คล้ายกันกับสัญญาณของที่เซลล์ นักวิจัยพบว่าอโต้ฟลูออเรสเซนต์เหล่านี้ส่วนใหญ่จะมีการต่อกันเป็นโครงสร้างขนาดใหญ่ในปริมาตรสามมิติ ในขณะที่เซลล์ที่ผู้วิจัยสนใจจะมีลักษณะอยู่แยกกันอย่างโคคเคียว ผู้วิจัยพัฒนาอัลกอริทึมซึ่งประกอบด้วยสองส่วนสำคัญ คือ ส่วนที่เป็นการตรวจจับสัญญาณของที่เซลล์ และส่วนการกำจัดสัญญาณอโต้ฟลูออเรสเซนต์ ส่วนแรกประกอบด้วยการทำ Thresholding กับข้อมูลภาพที่แปลงโดย Mexican hat filtering และ Top-hat transformation ส่วนที่สองเป็นการหาค่าความหนาแน่นของวอกเซลในสามมิติผ่านการทำ Mean Inter-Particle Distance (MIPD) เพื่อกำจัดสัญญาณรบกวน ในการศึกษาที่ผู้วิจัยได้ใช้ข้อมูลเซลล์ปลอมและข้อมูลจริงเพื่อทดสอบประสิทธิภาพของอัลกอริทึม เราพบว่าอโต้ฟลูออเรสเซนต์และเซลล์สามารถแยกกันได้ในโดยใช้ MIPD ผู้วิจัยพบว่า Sensitivity และ Specificity ของการตรวจหาสัญญาณเซลล์อยู่ที่ประมาณ 80-90% และ 98% ตามลำดับ โดยสรุปผู้วิจัยพัฒนาอัลกอริทึมสำหรับการตรวจหาสัญญาณเซลล์และกำจัดอโต้ฟลูออเรสเซนต์ส่วนใหญ่ที่มีลักษณะเป็นโครงสร้างได้อย่างมีประสิทธิภาพ ผู้วิจัยเชื่อว่างานวิจัยนี้เป็นการพัฒนาต่อยอดความสามารถและประสิทธิภาพของเทคโนโลยีโคร โออิมเมจจึงให้มีความก้าวหน้าและมีความน่าเชื่อถือไปในอีกระดับหนึ่ง ผลลัพธ์นี้จะยังผลให้เทคโนโลยีดังกล่าวเป็นที่รู้จักมากขึ้นต่อวงการวิทยาศาสตร์การแพทย์ทั้งในและต่างประเทศในอนาคตอันใกล้ และจะเป็นประโยชน์ต่อการพัฒนางานวิจัยในสัตว์ทดลองขนาดเล็กในภายภาคหน้าเป็นอย่างมาก

Thesis Title	A Novel Algorithm for Detecting Isolated Green Fluorescently-Labeled Cells in Cryo-imaging Data
Author	Mr. Thanapong Chatboonward
Degree	Master of Engineering (Biomedical Engineering)
Advisor	Asst. Prof. Dr. Patiwet Wuttisarnwattana

ABSTRACT

Cryo-imaging is a biomedical imaging technology for studying cellular biodistribution in small animal models. It can be used to locate cells of interest anywhere in a whole animal scale with single cell sensitivity. In this study, we are interested in green fluorescently labeled T-cells in the liver of the Graft-versus-Host disease mouse model. However, the detection of green fluorescently labeled cells is quite highly challenging and difficult due to the autofluorescence in the liver, especially bile duct and gall bladder. They have the same spectrum as the signal of T-cells. We observed that autofluorescence mostly tended to form into the dense structure in 3D volume whereas the cell signals of interest were distributed and isolated throughout the liver tissue. We developed an algorithm that consisted of two essential parts: the T-cell signal detection and the removal of the autofluorescent signals. The detection part consisted of thresholding on imaging data converted by Mexican hat filtering and Top-hat transformation. The second part was measuring the voxel density in 3D space with Mean Inter-Particle Distance for eliminating noises. In this study, we used both synthetic data and real data to test the algorithm performance. We found that the sensitivity and specificity of detection were around 80-90% and 98%, respectively. In conclusion, we successfully developed an algorithm for detecting green fluorescently labeled cells and cleaning the structured autofluorescent signals for the first time. We believe that this research is a further development of the capability and efficiency of Cryo-imaging technology. As a result, the technology should become more well-known to the medical science community, and it will greatly benefit the development of small animal research in the future.

CONTENTS

	Page
Acknowledgement	c
Abstract in Thai	d
Abstract in English	e
List of Tables	h
List of Figures	i
List of Abbreviations	k
List of Symbols	l
Glossary	m
Introduction	1
1.1 Introduction	1
1.2 Cryo-imaging study of a T-cell biodistribution in a graft-versus-host disease Mouse model	5
1.3 Significance of the research	6
1.4 Purpose of the study	7
1.5 Scope of the research	7
Literature reviews	9
2.1 Stem cell detection in Cryo-imaging	9
2.2 Cryo-imaging and microspheres-based blood flow	11
2.3 High spatial resolution measurements of organ blood flow in small laboratory animals	12
Experiment methods	14
3.1 Cryo-imaging Data	14
3.2 Green Cell Detection	15
3.3 Tissue mask Creation	18
3.4 Autofluorescent Cleaning	18
3.5 Synthetic Cells	20
3.6 Effect of k and $MIPD$ threshold values on the algorithm performance	22
3.7 Algorithm testing using synthetic data	22
3.8 Algorithm testing using real data	23
3.9 Workstation	23

Results and discussion	24
Summary	34
References	36
CURRICULUM VITAE	40



ลิขสิทธิ์มหาวิทยาลัยเชียงใหม่
Copyright© by Chiang Mai University
All rights reserved

LIST OF TABLES

	Page	
Table I	Algorithm performance in liver control 1	27
Table II	Algorithm performance in liver control 2	28
Table III	The number of green fluorescently labeled cell detections	32



ลิขสิทธิ์มหาวิทยาลัยเชียงใหม่
Copyright© by Chiang Mai University
All rights reserved

LIST OF FIGURES

	Page
Figure 1.1 High-resolution Cryo-image of whole mouse	2
Figure 1.2 3D visualization of Cryo-images	2
Figure 1.3 Cryo-imaging system	3
Figure 1.4 Color brightfield images and molecular fluorescent images of whole mouse	4
Figure 1.5 Cryo-imaging system output	4
Figure 1.6 Biodistribution in Cryo-imaging system	5
Figure 1.7 Liver fluorescent image in mouse model	7
Figure 2.1 Anatomical color brightfield and molecular fluorescence images with Cryo-imaging	10
Figure 2.2 Sombrero filtering and top-hat transformation in fluorescent images	10
Figure 2.3 Cell detection in the binary image by a supervised classifier	11
Figure 2.4 Cryo-images and processing for microsphere-based blood flow measurement	12
Figure 2.5 2D contour map of blood flow using microsphere density method	13
Figure 3.1 A single fluorescent, brightfield cryo-image and surface rendering of the liver	14
Figure 3.2 An isolated green fluorescently labeled cell signal	15
Figure 3.3 Sombrero filtering and top-hat transformation in fluorescent images	16
Figure 3.4 The candidate pixels and the green cells	17
Figure 3.5 Fluorescent image and tissue mask of the liver tissue	18
Figure 3.6 Proposed autofluorescent cleaning algorithm pseudocode	20
Figure 3.7 Green fluorescently labeled T-cells and synthetic cells	21
Figure 4.1 Surface rendering of the results generated by the green cell detection algorithm	24
Figure 4.2 The relationship between the <i>normalized error</i> , and the parameters, k and <i>MIPD</i> thresholds	25
Figure 4.3 The image analysis of liver cryo-images with synthetic cells	26
Figure 4.4 The relationship between sensitivity and cell density and specificity and cell density	28

Figure 4.5 The false negative results or the synthetic cells that were removed and the autofluorescent noises that were removed after the cleaning process	29
Figure 4.6 The image analysis of five different liver cryo-images with green fluorescently labeled cells	30
Figure 4.7 The image analysis of the liver voided of cell signal	33



ลิขสิทธิ์มหาวิทยาลัยเชียงใหม่
Copyright© by Chiang Mai University
All rights reserved

LIST OF ABBREVIATIONS

CFSE	Carboxyfluorescein Succinimidyl Ester
CT	Computerized Tomography
GVHD	Graft-Versus-Host Disease
hMSCs	human Mesenchymal Stem Cells
IACUC	Institutional Animal Care and Use Committee
-LoG	inverted Laplacian of Gaussian
MAPCs	Multipotent Adult Progenitor Cells
MIPD	Mean Inter-Particle Distance
MRI	Magnetic Resonance Imaging
OCT	Optimal Cutting Temperature
PET	Positron Emission Tomography
SNR	Signal to Noise Ratio
TP	True Positive
FN	False Negative
FP	False Positive
USA	United State of America



ลิขสิทธิ์มหาวิทยาลัยเชียงใหม่
Copyright© by Chiang Mai University
All rights reserved

LIST OF SYMBOLS

σ	Lower case Sigma, Gaussian spreadness parameter
Σ	Upper case Sigma, Summation
λ	Lambda, Small mean value
δ	Delta, Standard deviation
β	Beta, Standardized coefficients



ลิขสิทธิ์มหาวิทยาลัยเชียงใหม่
Copyright© by Chiang Mai University
All rights reserved

GLOSSARY

Autofluorescence	Green spectrum light emitted by biological organelles such as, lysosomes and mitochondria.
CFSE	Carboxyfluorescein Succinimidyl Ester, A fluorescent dye for cell staining.
Cryo-imaging	A biomedical imaging technology for studying cellular biodistribution in small animal models.
Euclidean distance	A distance between two voxels in 3D volumetric data.
GVHD	Graft-Versus-Host Disease, a condition that the donor T-cells recognize the recipient as foreign after an allogeneic transplant.
K -d tree	A K -dimensional tree for organizing data structure in K -dimensional space.
k nearest neighbors	An algorithm for finding the k nearest neighbor.
Mexican hat filtering	A image processing technique used for detecting bright signals.
<i>MIPD</i>	Mean Inter-Particle Distance, an averaged distance measured by averaging the distance from voxel of interest to other voxels.
OCT gel	Optimal cutting temperature gel, a glycol and resin-based compound gel used for dipping the small animal samples in cryo-imaging system.
Synthetic cells	The synthetic data that was created for imitating the real cells.
T-cells	One of the important types of white blood cells that plays a crucial role in the immune system.
Top-hat transform	A morphological image processing technique used for extracting small elements and details.

Chapter 1

Introduction

1. Introduction

Biomedical imaging technologies have an important role in clinical diagnosis due to some examinations, especially the internal organs of the body that are not easily accessible. Many imaging technologies, including, Computerized tomography (CT), Magnetic resonance imaging (MRI), Positron emission tomography (PET), and bioluminescence imaging are widely used in both medical diagnosis and molecular imaging studies [1]. Each has unique features for different clinical diagnoses. CT scan is best for imaging bones [2]. It can also perform vascular imaging if a contrast agent is used [3]. MRI is capable of distinguishing soft tissues such as gray matter and white matter in the brain. It is best for separating watery and fatty tissues. MRI is used clinically such as neurological diseases [4], cardiovascular diseases [5], musculoskeletal diseases [6], and oncological diseases [7]. PET is mainly used for functional imaging such as metabolism imaging [8], cancer biology [9], perfusion imaging [10], and cardiovascular diseases [11]. Bioluminescence imaging is specifically used pre-clinically in transgenic mice. The cells of interest are genetically modified to produce proteins that can chemically produce light similar to the process observed in fireflies [12]. Although, all these techniques can provide whole animal scale imaging, they have some critical limitations. One of these is that they cannot provide a single cell sensitivity over a large volume of a small animal. This feature can be observed in intravital imaging or phase contrast imaging [13, 14]. But still, these two cannot provide whole animal imaging because they have a limited field of view.

Cryo-imaging is the only technology that amazingly overcomes these limitations as it provides whole animal scale imaging with single cell sensitivity. Cryo-imaging can provide a high-resolution 3D volume of a whole mouse and internal organs (Figure. 1.1-1.2). Cryo-imaging has been used to study cellular biodistribution in small animal models [15-17], co-localization of various cell types in different tissues [18], cancer metastasis studies [19], cardiovascular disease treatments [20], and more [21].

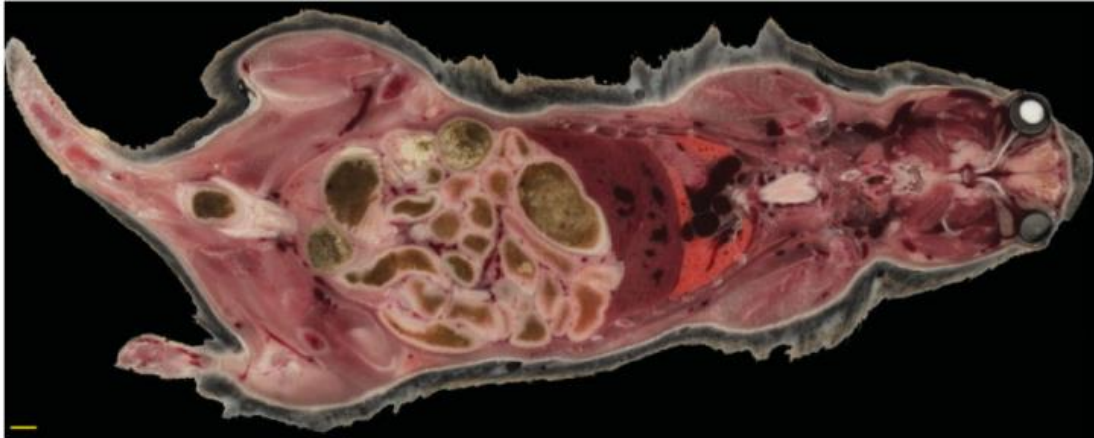


Figure 1.1 Cryo-imaging provides high resolution cryo-image of the whole mouse. The coronal section of the cryo-image is observed for clearly identifying major organs such as lungs, liver, heart, stomach, intestine, and colon. [22]

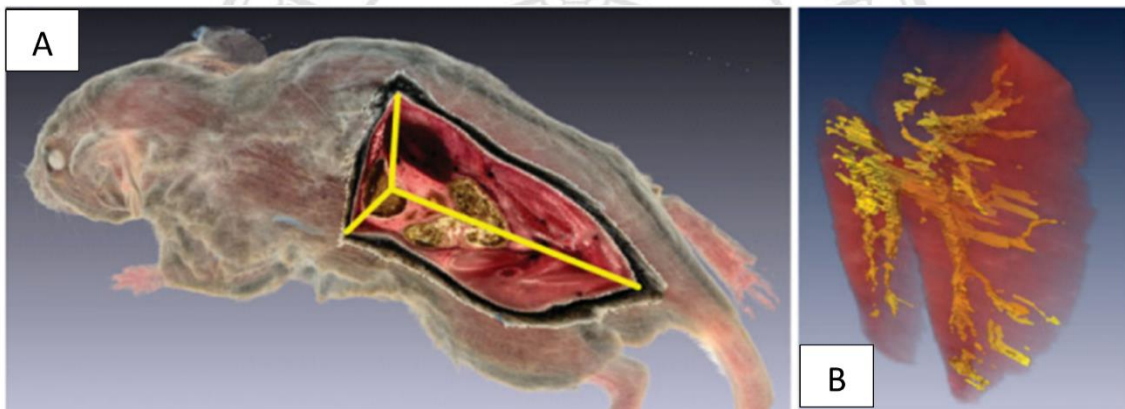


Figure 1.2 shows the 3D visualization of cryo-images. (A) 2D coronal sections shown in figure 1.2 are visualized in the 3D volume of the whole mouse. Cryo-imaging can also provide 3D reconstructed of segmented organs such as segmented lungs with internal vasculature (B). [22]

Cryo-imaging is designed and developed by the research group led by David L. Wilson [23]. The developed cryo-imaging system can provide high-resolution 3D volumetric imaging data on the whole small animal body. It produces high resolution anatomical brightfield and molecular fluorescent images and it can also be seen at the level of single fluorescent cells anywhere. This unique feature has not been observed in any other biomedical instruments before. Cryo-imaging consists of a built-in automatic cutter and a tiled microscope imaging system (Figure 1.3B) including, a whole mouse cryo-microtome (Figure 1.3A) cabinet which operates at -20°C and the automated-3-axes stepper control (Figure 1.3D) which moves the microscope in the proper position. The cryo-imaging system is shown in Figure 1.3. The first step in the cryo-imaging starts with dipping the mouse samples with OCT (Optimal Cutting Temperature) gel, which is a

glycol and resin-based compound. The sample is immersed and hardened using liquid nitrogen. After the mouse sample is solidified, it is then firmly fixed on the cutting stage to prevent the sample from moving out of the proper position. When the mouse sample is attached to the cutting stage (Figure 1.3H), the stage begins to move back and forth, and the blade (Figure 1.3G) begins to slice the sample into a very thin sheet. The microscope on the top of the system then starts to image the block face. The process of slicing and imaging is continuously repeated until the entire mouse sample is completely gone. Both brightfield (Figure 1.4A) and fluorescent images (Figure 1.4B) are obtained during the process. The cryo-imaging takes approximately 12 hours to complete the entire mouse imaging. All the image data can be visualized in 3D volumetric data and can be extracted for the 3D segmented organs as shown in figure 1.5.

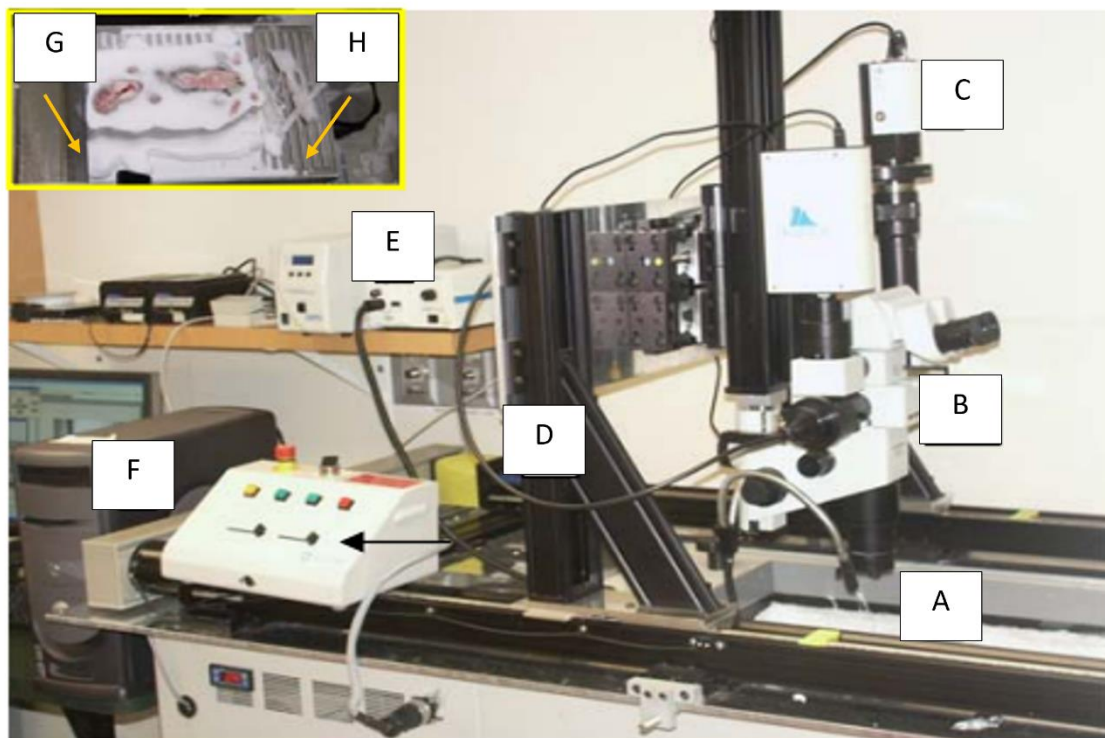


Figure 1.3 Cryo-imaging is a sectioning-and-imaging system for small animal models. The system consists of a cryo-microtome (A), tiled microscope (B), low-noise camera (C), stepper control (D), illuminators (E), and control computer (F). Figure 1.3H. shows the cutting stage with OCT embedded mouse sample. The cutting stage will move back and forth, and the blade (G) will slice the mouse sample into a very thin sheet. [22]

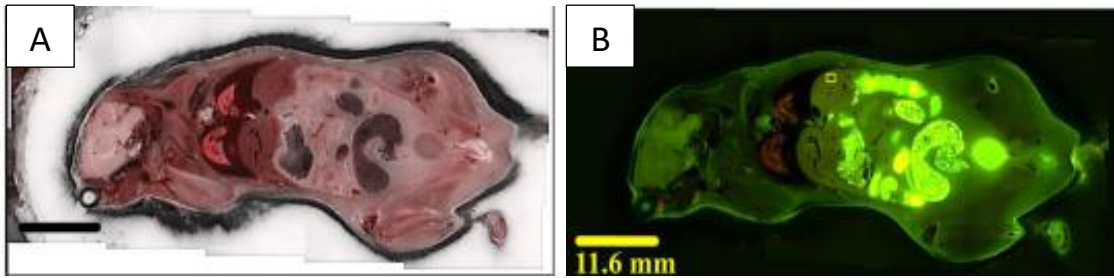


Figure 1.4 Cryo-imaging provides high resolution color brightfield images (A) and molecular fluorescent images (B) of the whole mouse. [15]

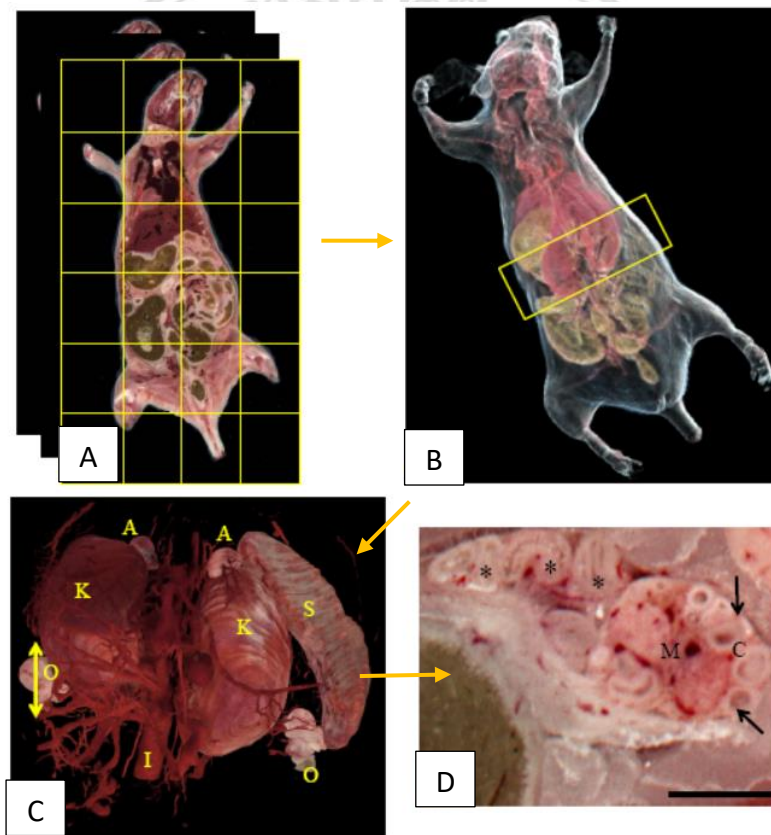


Figure 1.5 Cryo-imaging system provides tiled imaging of the whole mouse and stitches the 2D tiled cryo-images into 3D volume (A). The 3D visualization of cryo-images can provide both physical and molecular fluorescence data of the whole mouse (B). The internal organs of interest can also be extracted and seen in any position (C) including, zooming at the cellular level (D). [24]

2. Cryo-imaging study of a T-cell biodistribution in a graft-versus-host disease mouse model

In previous reports [15-18], Wuttisarnwattana and his colleagues studied the biodistribution of stem cells and T-cells in graft-versus-host disease (GVHD) mouse model. They hypothesized that mesenchymal stem cells could alleviate GVHD symptoms in the mouse model. They tracked where these cells went after the intravenous injection using cryo-imaging. To track these cells under the cryo-imaging system, the stem cells were labeled with red fluorescent dyes while the T-cells were labeled with green fluorescent dyes. 3D visualization results showed that cryo-imaging was enabled to study both stem cell and T-cell biodistribution in a whole mouse scale with single cell sensitivity as shown in figure 1.6. They found that stem cells and T-cells were tracked and co-localized in both secondary lymphoid organs such as, spleen and lymph nodes and GVHD target organs such as lung, liver, skin, G.I. tract, and thymus after intravenous injection. These key organs were the locations where hMSCs (human mesenchymal stem cells) immunomodulation occurred [18]. This is the first time that biodistributions of stem cells and T-cells in the mouse model were qualitatively and quantitatively identified. However, the quantification of the green fluorescently T-cells has not yet been established.

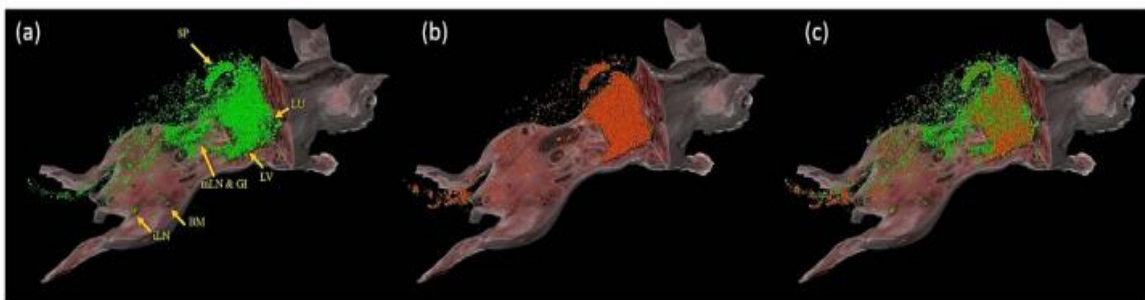


Figure 1.6 Cryo-imaging system enables to visualize stem cell (b) and T-cell (a) tracking and co-localize (c) in a whole mouse scale with single cell sensitivity. Both red labeled stem cells and green fluorescently labeled T-cells were significantly detected in the secondary lymphoid organs and GVHD target organs. They were mostly located in spleen (SP), lung (LU), liver (LV), mesenteric lymph nodes and G.I. tract (mLN & GI), femur bone marrow (BM), and inguinal lymph nodes (iLN). [25]

3. Significance of the research

Although the previous studies could identify the red fluorescently labeled stem cells in various organs of the mouse model, the missing story is to establish the T-cell biodistribution. T-cell is one of the essential immunological cells, that has various functions. For example, responding to pathogens or foreign substances, balancing immune homeostasis, responding to inflammation, and more. T-cells also play a crucial role in GVHD development [26]. Since the donor T-cells recognize the recipient as foreign, the recipient's immune cells are unable to resist donor T-cells and induce a GVHD development. Therefore T-cell biodistribution study is needed. The problem is to analyze the green fluorescently T-cells in different organs, especially with highly autofluorescence like the liver. Autofluorescence naturally occurs in almost all animal tissues, especially in connective tissues [27, 28]. The emission of autofluorescent light is from a biological structure such as elastin and collagen. It is well known that bile produced in the liver and other connective tissues have highly autofluorescence in the green spectrum as captured by cryo-imaging (Figure 1.7) [29]. It is extremely difficult to distinguish between the green cells and those autofluorescence. By counting the green T-cells in the liver volume, the results significantly contain false positives that make the results unreliable. Thus, we need an algorithm capable of eliminating the autofluorescence or noises but preserving the green cell signals. To best of our knowledge, there is no such algorithm published to solve this specific problem before. Hence, this project is significant.

ลิขสิทธิ์มหาวิทยาลัยเชียงใหม่
Copyright© by Chiang Mai University
All rights reserved

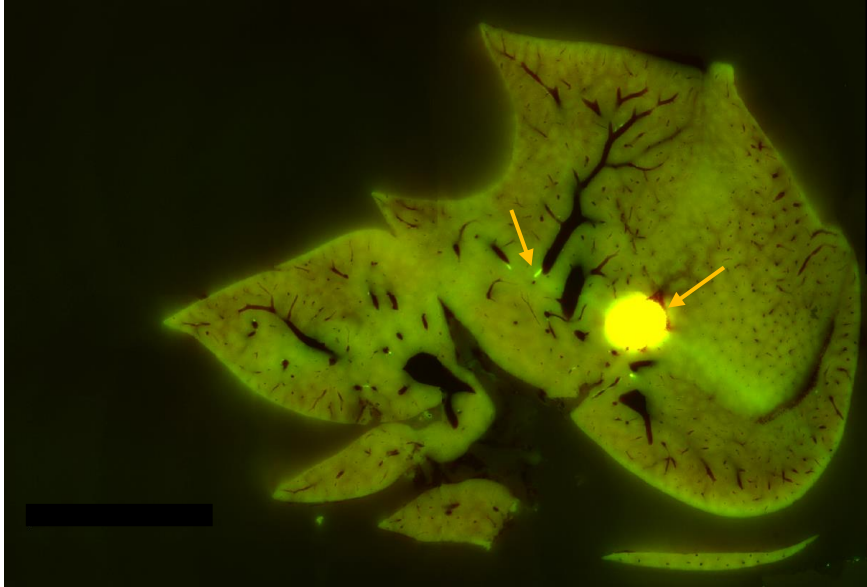


Figure 1.7 Liver fluorescent image of a mouse model showed a high autofluorescence emitted by bile and other connective tissues. The left arrow is the bile duct, and the right arrow is the gall bladder. Both bile duct and gall bladder produce most of the highly autofluorescence in the liver. (Unpublished)

4. Purpose of the study

1. To develop an algorithm for detecting isolated green fluorescently labeled cells in liver mouse cryo-imaging data.
2. To reduce the autofluorescent signals in the liver data that mainly comes from the biliary tract. These signals are supposedly noises that may interfere with the quantification of the green fluorescently labeled cells.

5. Scope of the research

1. The cryo-imaging dataset used in this study is the secondary source from previous studies and is authorized to use by Prof. David L. Wilson of Case Western Reserve University, USA. The details of the experiment and the imaging protocol can be read in the previous studies [23].

2. The algorithm is created specifically for detecting green fluorescently labeled T-cells in livers. The T-cells are assumed to be scattered and isolated in the tissue of interest. Clustered T-cells are not considered in this study.



ลิขสิทธิ์มหาวิทยาลัยเชียงใหม่
Copyright© by Chiang Mai University
All rights reserved

Chapter 2

Literature Reviews

1. Stem cell detection in Cryo-imaging

In a previous study [15], Wuttisarnwattana and his colleagues developed a robust algorithm for stem cell detection in cryo-images of mouse models. They used a cryo-imaging system to study stem cell biodistribution and track stem cells in the whole mouse models with single cell sensitivity. The stem cells used in this study were multipotent adult progenitor cells (MAPCs) and they were labeled with red quantum dot dye (Figure 2.1). The stem cells appeared as red spots in fluorescent cryo-images. They proposed their novel algorithm for detecting red labeled stem cells in cryo-images. The first step of the algorithm was to eliminate nonessential regions (such as fur, embedding medium, and G.I. tract) to reduce number of pixels in consideration. They then extracted the stem cell features in fluorescent images using sombrero filtering and top-hat transformation (Figure 2.2). These techniques were used to maximize the cell signals and suppress the background signals. They identified the candidate pixels using thresholding rules of the extracted features. They then classified the candidate pixels as either cells or background by using the bagged decision trees [30]. Finally, they segmented the complete cell patches from the fluorescent volume (Figure 2.3). This new algorithm could accurately detect and quantify the stem cell signals. The contribution of this research was the uniqueness of tracking cells with single cell sensitivity on a whole mouse scale for the first time.

ลิขสิทธิ์มหาวิทยาลัยเชียงใหม่
Copyright© by Chiang Mai University
All rights reserved

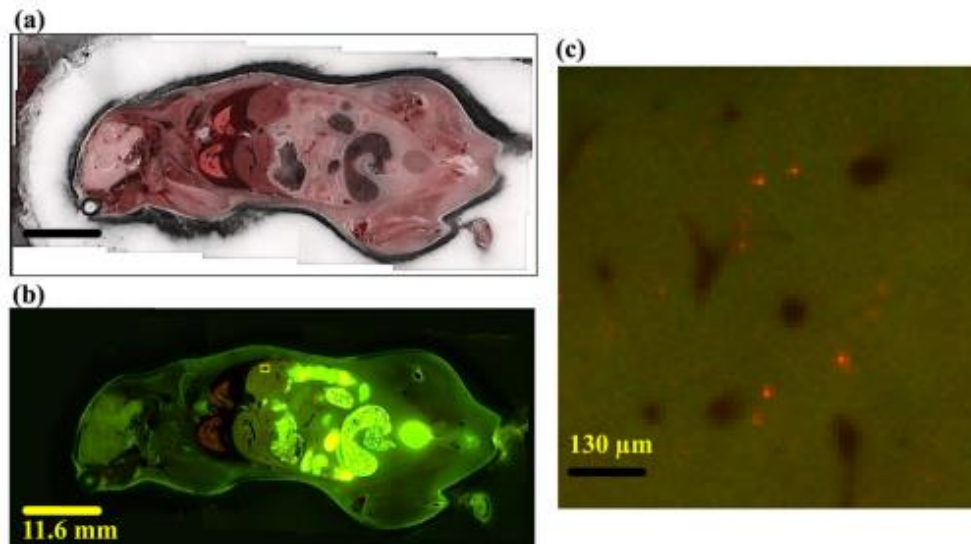


Figure 2.1 Cryo-imaging enables the provision of anatomical color brightfield (a) and molecular fluorescence (b) images in great detail. It can be used to detect red quantum dot stem cells (c) anywhere in a whole mouse with single cell sensitivity. [15]

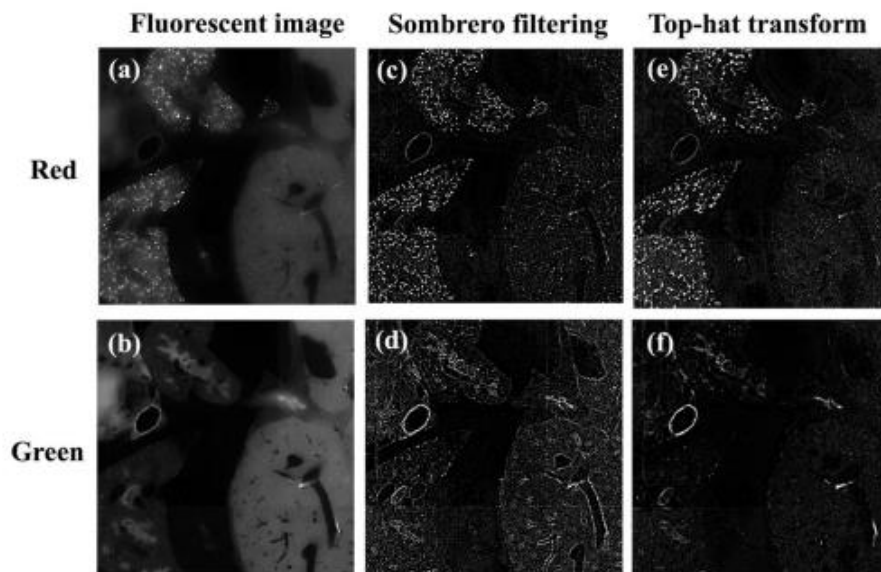


Figure 2.2 Sombrero filtering and top-hat transformation were applied to both red (a) and green (b) fluorescent images for extracting cell features. Sombrero filtering was used to detect bright fluorescent cells in red (c) and green (b) channel. Top-hat transformation was used to separate small elements and details from the red (e) and green (f) fluorescent images. [15]

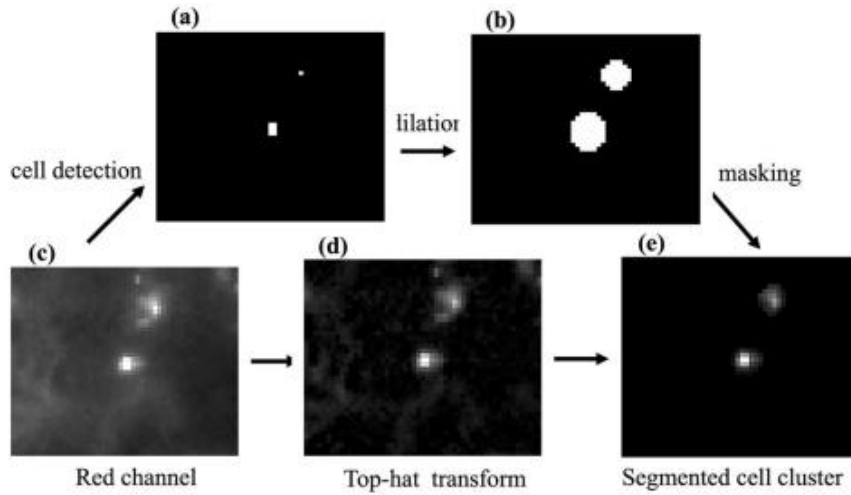


Figure 2.3 A supervised classifier provides cell detection in a binary image (a) as output. The binary image is used to dilate and identify the segmented cluster (b). It is used to mask the top-hat transformation (d) in the red channel (c). A segmented cell cluster is provided as the result in grayscale (e). [15]

2. Cryo-imaging and microspheres-based blood flow

In a previous study [31], the researchers compared myocardial perfusion imaging using CT estimations of quantitative blood flow to fluorescent microsphere cryo-images in porcine ischemic model. They inserted the balloon for inducing ischemia and measuring the extent of ischemia. They used fluorescent microspheres to test myocardial blood flow. First, they injected red fluorescent microspheres and collected a blood sample. Second, they used the inflated balloon to induce a stable ischemia. They then injected green fluorescent microspheres and collected a separate blood sample. After that, the animal was taken to the CT scanner for a dynamic myocardial perfusion imaging CT scan and analyzed for blood flow quantification. They then used the Cryo-imaging to acquire both brightfield and fluorescent images. They measured myocardial blood flow in the cryo-images by microspheres density methods. The microspheres density is defined as:

$$\left(\frac{Flow}{Volume}\right)_{tissue} = \frac{\left(\frac{Count}{Volume}\right)_{tissue}}{Count_{blood}} * Rate_{blood}$$

Where $(\frac{Count}{Volume})_{tissue}$ is the microsphere count density in the myocardium measured by Cryo-imaging, $Count_{blood}$ is the microsphere count in the collected blood samples measured by flow cytometry, and $Rate_{blood}$ is the withdraw rate of the collected blood sample. Finally, the detected images of both red and green microspheres were acquired. The cryo-images showed the microspheres-based blood flow quantification as shown on Figure 2.4. Figures 2.4c and 2.4e show that the left anterior descending (LAD) coronary artery is clear. Figures 2.4d and 2.4f show hemodynamically stenosis in the LAD. By measuring microsphere density method, we hypothesized that this density method could be applied to our research.

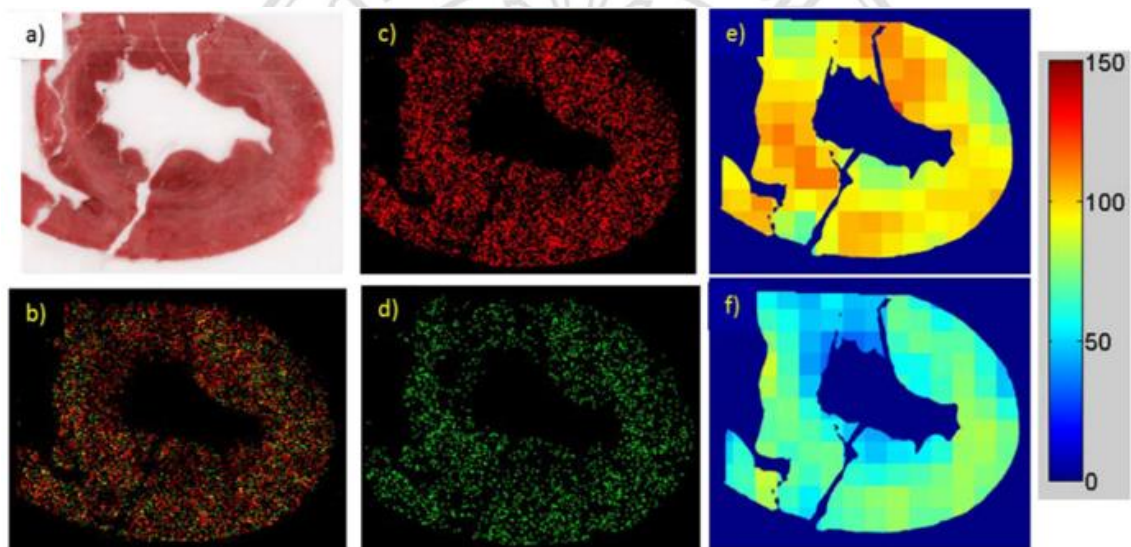


Figure 2.4 Cryo-images and processing for microsphere-based blood flow measurement as an example. (a) Anatomical data and tissue segmentation from a brightfield image. (b) fluorescent images of red and green microspheres. (c) Red microspheres have been identified. Green microspheres were detected in (d). For (e) red microspheres and (f) green microspheres, MBF maps were obtained by cryo-imaging.

3. High spatial resolution measurements of organ blood flow in small laboratory animals

In another study [32], the researchers used fluorescent microspheres to test blood flow distribution within the organs of a small animal. They dissected the organs and measured blood flow distribution in those organs. They created the tree structure and stored the spatial coordinates of all microspheres to determine the distance between microspheres. They observed that there were more microspheres in higher blood flow locations than in

lower blood flow locations. The higher the density of microspheres distributed in that location, the lower the mean of the nearest microsphere distance measured. Therefore, the mean of the nearest microsphere distance is proportional to the blood flow. They found that the density measure of microspheres represented the spatial distribution of blood flow in the organ. With the microsphere density method, they visualized the spatial distribution of blood flow using contour maps (Figure 2.5). The point of interest in this study was that they used Mean inter-particle distance (*MIPD*) to quantify the density of microspheres in blood flow. This density method was successfully used to estimate the quantitative distribution of microspheres and blood flow in the organs. Thus, we applied the same principles to our research using *MIPD* as the density method.

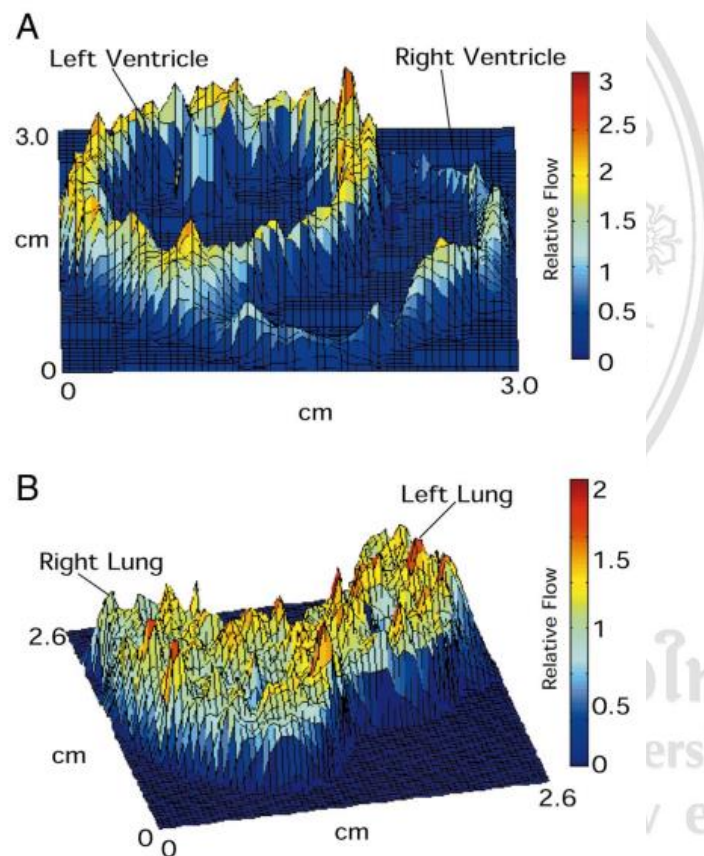


Figure 2.5 represents a 2D contour map of blood flow in rabbit heart and rat lung using the microsphere density method. The higher the density of microspheres, the higher the relative blood flow in that location. [32]

Chapter 3

Experiment methods

1. Cryo-imaging Data

Cryo-imaging data used in this study were the secondary data from a another study [15]. We were authorized to use the data by Prof. David. L. Wilson, a director of the biomedical laboratory at Case Western Reserve University, USA, and all animal experiments were approved by the Institutional Animal Care and Use Committee (IACUC) at Case Western Reserve University, USA. The main purpose of this research was to study the biodistribution of alloreactive T-cells in a GVHD mouse model using cryo-imaging. However, in this study, we focused only on analyzing the livers of the mouse data. Figure 3.1 showed a single cryo-imaging slice of the liver as well as a surface rendering of the liver. T-cells in this study were stained with a green fluorescent dye which was carboxyfluorescein succinimidyl ester (CFSE). The CFSE dye is a well-known fluorescent dye used for studying lymphocyte proliferation [33]. CFSE is a cell-permeable dye and is covalently bound to intracellular molecules of T-cells via CFSE's succinimidyl group [17]. T-cells uptake CFSE dye and appeared green in the fluorescent image. With the optical setting, the cell signal appeared as green spots in the fluorescent image (Figure 3.2). Details of the experiments and the findings are outlined in the original papers [15-18].

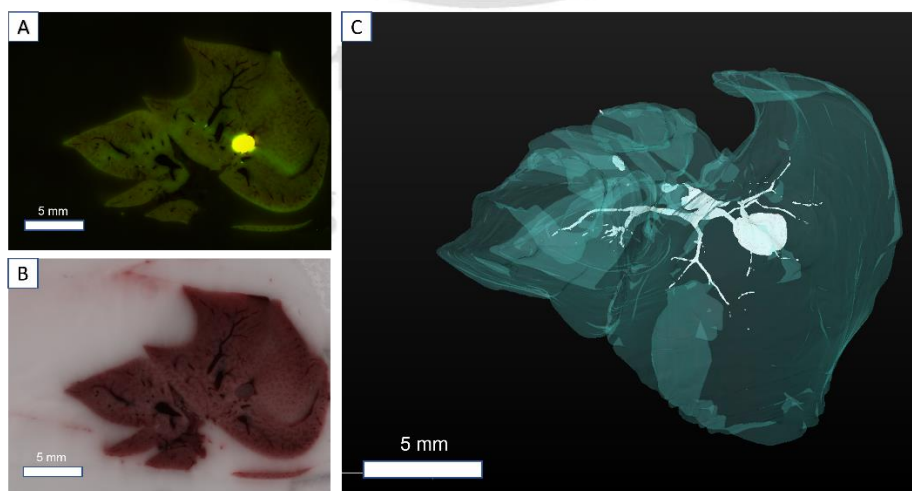


Figure 3.1 showed a single fluorescent (A), brightfield (B) cryo-imaging slice, and surface rendering (C) of the liver.

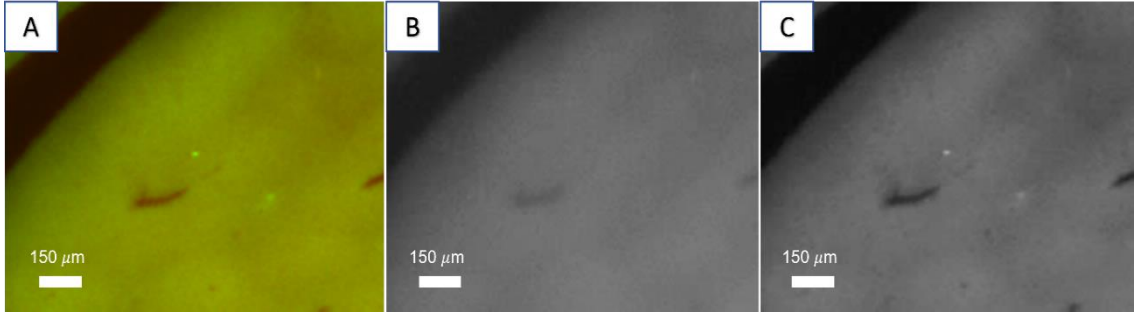


Figure 3.2 Example of an isolated green fluorescently labeled cell signal. In this experiment, T-cells were labeled with green fluorescent dyes and intravenously injected into a mouse. T-cells could be found in many organs, including the liver (A). Interestingly, the signal of green cells appeared in the green channel (B) but not in the red channel (C).

2. Green Cell Detection

In this study, T cells were seen as tiny pixels and the details inside the cell were not visible because of the magnification of the microscope. Since this study was designed to investigate the whole animal scale, the magnification was set to scope the whole animal scale. So, the details of cells such as the nucleus were not seen. Cell signals of interest could be seen as the green spots against a greenish background in the fluorescent images (Figure 3.2). We observed that signals of the green cells (T-cells) appeared in the green channel but not in the red channel of the fluorescent image. The algorithm should be able to distinguish between pixels of the green cells and pixels of the background. As inspired by the previous study [15], we employed Mexican hat filtering and top-hat transformation to extract cell features in each fluorescent image. Both spatial filters are capable of maximizing the cell signals while suppressing the background signals. Mexican hat filtering, also known as inverted Laplacian of Gaussian ($-LoG$), is defined as:

$$Filtered\ I = I * (-LoG(\sigma_{filter})) \quad (1)$$

where $*$ represents as 2D correlation, $Filtered\ I$ is the fluorescent image filtered by the Mexican hat filtering, I is the fluorescent image before filtering, LoG is a kernel that has the appropriate parameter σ_{filter} to calculate. The parameter is chosen to maximize the signal to noise ratio (SNR) value.

Top hat transformation is a digital image processing technique that is used to separate small elements and details against a relatively homogenous background. The transformation is defined as:

$$tI = I - (I \circ Disk(R_{filter})) \quad (2)$$

where \circ represents as grayscale morphological opening, tI is the fluorescent image filtered by top hat transformation, I is the fluorescent image before filtering, $Disk(R_{filter})$ is the disk structuring element that has R_{filter} as a radius.

In this study, we only used red and green channels of RGB fluorescent images because the fluorescent excitation light was in the blue spectrum so the blue channel was filtered out during the fluorescent image acquisition. Thus, we applied the Mexican hat filtering and the top-hat transformation to red and green channels of the RGB fluorescent image, giving a total of four extracted features (Figure 3.3).

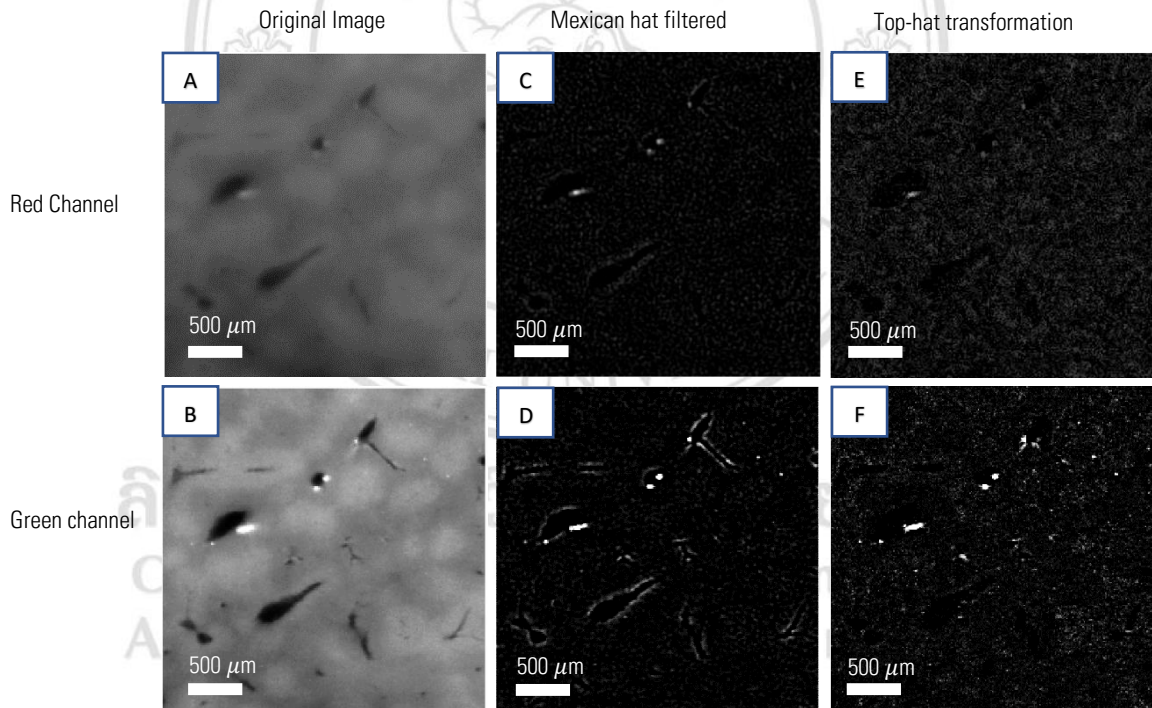


Figure 3.3 Green cell signals are not appeared in the red channel (A) but appeared in the green channel (B) of the fluorescent image. We performed feature extraction to the green cell signals giving 4 features in total: Mexican hat filtering of the red channel (C) and the green channel (D), Top-hat transformation of the red channel (E), and the green channel (F).

After applying Mexican hat filtering and top hat transformation, we then identify the candidate pixels which represent the pixels that are very likely to be the green cells. This can be done simply by applying thresholds to the extracted features. This technique

is based on an assumption that signals of the green cells appear only in the green channel, but not in the red channel. Also, most of the autofluorescence signals appear in both red and green channels (Figure 3.3). Autofluorescence signals usually come from bile ducts, gall bladder, and other connective tissues. Therefore, a candidate pixel is defined as a pixel that has strong signals in both extracted features of the green channel, and it must also have the green composition be greater than the red composition. This can be translated into an equation:

$$Candidates = (fG > T_{fG}) \cap (tG > T_{tG}) \cap (tG > tR) \cap Tissue\ masks \quad (3)$$

where fG represents the Mexican hat filtered green feature, tG represents the top-hat transformed green feature, tR is the top-hat transformed red feature, T_{fG} and T_{tG} are threshold values for selecting the bright green signals, and $Candidates$ are the pixels with a high probability of being the green cells. $Tissue\ masks$ are the binary images of liver tissues used to exclude the irrelevant parts of liver tissues. Note that this process can significantly reduce the number of pixels in consideration as compared to processing the whole image (Figure 3.4).

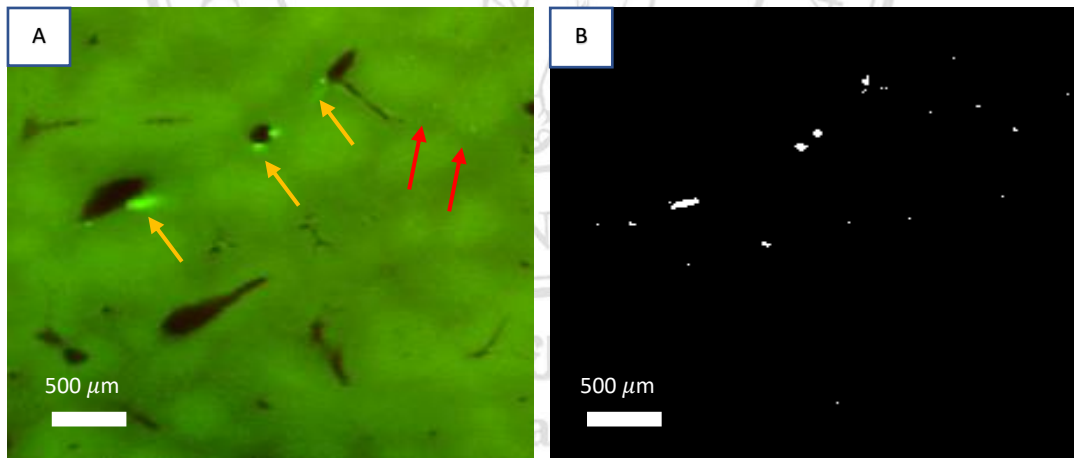


Figure 3.4 We identify the candidate pixels that potentially are the green cells. This can be done by applying thresholding to the four extracted features. It could significantly reduce the number of background pixels that are not green cells for further processing. Fig A shows the original liver image with isolated fluorescently labeled cells and Fig B shows the results of the candidate pixels in a binary image. The yellow arrows indicate the autofluorescence signals and the red arrows indicate the green cell signals.

3. Tissue mask creation

A tissue mask is used to remove immaterial parts outside liver tissues. We manually created tissue masks by hand drawing using Amira software (Thermo Fisher Scientific). First, we loaded fluorescent images of liver tissue (Figure 3.5A). We then made a drawing according to the shape of liver tissue. We repeated the manual segmentation process to all images in the liver. In total, we had 7 livers in this study. An example of a fluorescent slice of a liver and the corresponding tissue mask are shown in figure 3.5.

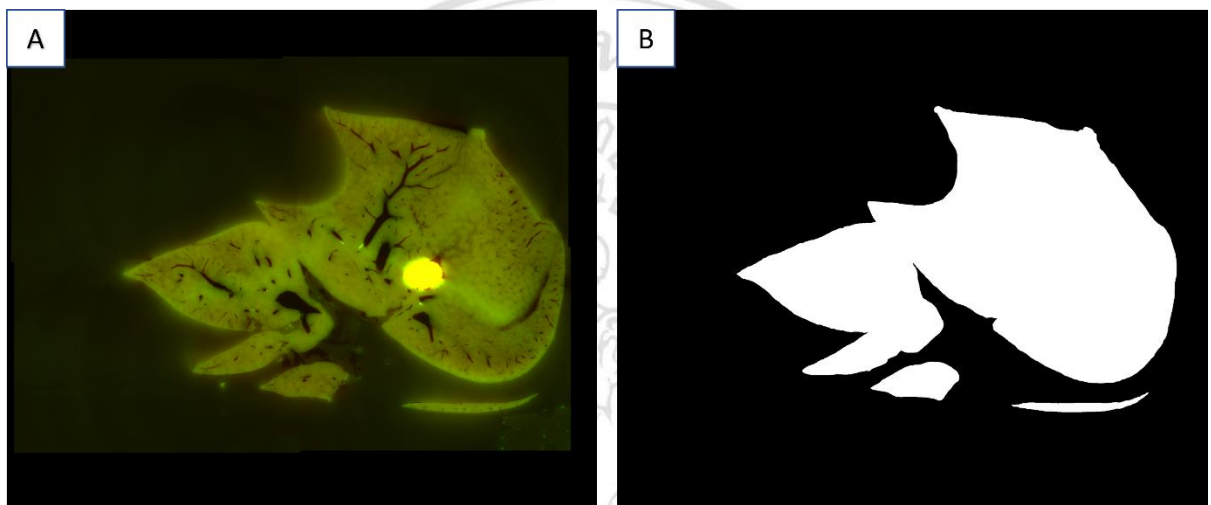


Figure 3.5. shows fluorescent image (A) and tissue mask (B) of the liver tissue.

4. Autofluorescence Cleaning

Green autofluorescence of the biliary tract and other tissues in fluorescent cryo-images of the liver tend to form large and dense structures in 3D volume. On the other hand, the green T-cells of interest tend to be isolated and spread throughout the liver tissues. For this reason, we expect that the 3D voxel density surrounding a voxel of interest can be used to distinguish between green cells vs. green autofluorescence (noises). Since we assume that the autofluorescent voxels reside close to each other and form dense structures, the voxel density among them should be very high. Therefore, we hypothesize that voxels of the isolated green cell should have a much lower voxel density as compared to those calculated from noises.

To measure the voxel density, we use mean inter-particle distance (*MIPD*) [32]. The *MIPD* is measured by averaging the distances from a voxel of interest to the k nearest voxels in 3D space. The *MIPD* is formulated as followed:

$$Distance_{ij} = \sqrt{(x_i - x_j)^2 + (y_i - y_j)^2 + 4^2(z_i - z_j)^2} \quad (4)$$

$$MIPD_i = \frac{1}{k} \sum_{j=1}^k Distance_{ij} \quad (5)$$

$Distance_{ij}$ represents the Euclidean distance of voxel i (x_i, y_i, z_i) to voxel j (x_j, y_j, z_j). $MIPD_i$ is the mean interparticle distance of voxel i to k nearest voxels ($j = 1 \dots k$). Please note that we have 4^2 in front of the z axis to account for anisotropic effect of the voxel dimension, i.e., the voxel size is $10 \mu\text{m} \times 10 \mu\text{m} \times 40 \mu\text{m}$.

Smaller *MIPD* indicates higher voxel density surrounding the voxel of interest which suggests that the voxel of interest is the autofluorescence (noises), that should be rejected. On the other hand, larger *MIPD* can be assumed to be a cell voxel, that should be preserved.

The k nearest neighbors algorithm can efficiently be implemented using the K -d tree data structure [34], where the searching complexity is reduced from $O(n^2)$ to $O(n \log n)$ and the K is 3 in our application. Please note that $K = 3$ represents a 3D spatial location, whereas k in the k nearest neighbor algorithm defines the number of nearest neighbors.

To clean autofluorescence signals, a voxel density threshold is applied to all detected voxels to determine whether those signals are noises. First, 3D spatial coordinates (x, y, z) are extracted from all candidate voxels to create a coordinate list. Second, the list is then used to create the K -D -tree data structure. Please note that the index coordinates must be converted to physical coordinates to determine the size of the anisotropic voxel (Equation 4). Our voxel resolution has an in-plane (or xy) resolution of $10.5 \mu\text{m}$, while the slice thickness (or z) is $40 \mu\text{m}$. Therefore, the distance of adjacent voxels in the same image (along xy axes) is not equal to the distance of different images (along z axis). Third, we iteratively calculate the *MIPD* for each voxel in the list. This can be done by averaging the Euclidean distances measured from the voxel to all k nearest neighbors (searching through the K -D tree, Equation 5). If the voxel's *MIPD* is less than

a predetermined threshold, we will consider the voxel to be autofluorescence noises and then eliminate it immediately. Finally, the remaining voxels will be dilated in 3D and applied with connected component analysis to count the number of cell detection. The pseudocode of the proposed algorithm is shown in figure 3.6.

```
For each fluorescent cryo-image
  Filter the image with Mexican hat filter and top hat transforms into the red and green channels
  Identify candidate pixels using thresholding
Stack the results in the 3D volume
Extract the physical coordinates of each voxel
Build the  $Kd$ -tree ( $K=3$ ) structure from the coordinate list
For each voxel in the list
  Find  $k$ -nearest neighbors and calculate the  $MIPD$ 
  If the  $MIPD$  threshold < a threshold, then remove the voxel
Perform 3D dilation and connect component analysis to quantify the number of remaining cells
```

Figure 3.6 Proposed autofluorescent cleaning algorithm pseudocode.

5. Synthetic Cells

We used synthetic cells that mimic the real model T-cells for evaluating the efficiency of our detection algorithm. The experiment's goal was to quantify the number of green cell signals in the liver data while suppressing any autofluorescence signals as well as other noises. Since we did not have a ground truth indicating the exact locations of the cells in livers, we created synthetic cells that were similar to the green fluorescently labeled cells in terms of, size, color, and brightness (Figure 3.7). Synthetic cells are uniformly distributed throughout liver tissues. If there are a cluster of synthetic cells, we will not consider it. Synthetic cells will be added to the control cryo-images that have no cell signals. Since we know the exact locations of the synthetic cells in the liver data, we can test for false positives and false negatives in our algorithm. If the locations of detected signals are not among the synthetic cell locations, the detections will be counted as false positives. On other hand, if the locations of synthetic cells are not among the detections, we will correspondingly increase the number of false negatives.

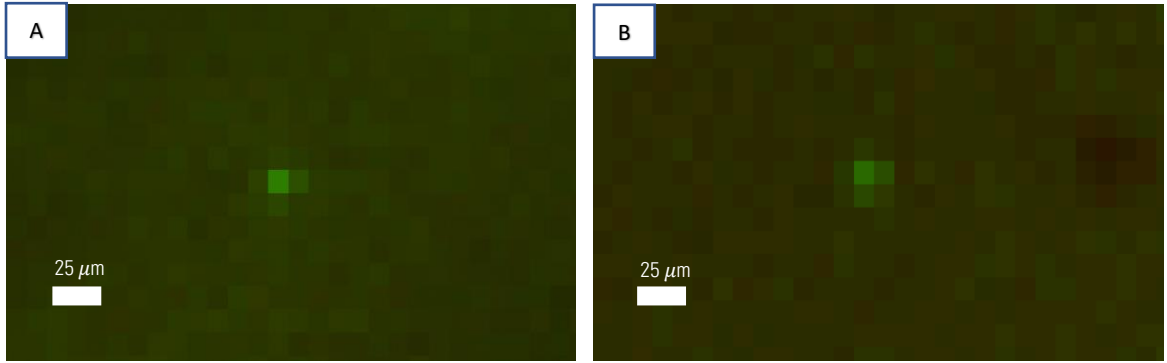


Figure 3.7 shows the similarity of green fluorescently labeled T-cells (A) and synthetic cells (B).

To create the synthetic cells. First, we loaded the liver volume that has no fluorescently labeled cells. We then eliminated the irrelevant area from the liver image data to prevent adding the synthetic cells into these areas. These areas include OCT area, lymph nodes, gall bladder, and other irrelevant tissues. After that, we randomized locations of N to be added to the fluorescent volume $((x_i, y_i, z_i) | i = 1, \dots, N)$. These locations are constrained to be within the relevant area are described above. We next added N synthetic cells to the fluorescence images in the origin locations by creating the random number of synthetic cells (n_i) from Poisson distribution that has small mean value λ . where n_i is the number of gaussian per cell patches. We then created the small random offsets for deciding the available locations of synthetic cells $((dx_j, dy_j) | j = 1, \dots, n_i)$ from Gaussian random generator that has standard deviation δ_{offset} and zero mean. We generated Gaussian intensity distribution $(G_j(x_i + dx_j, y_i + dy, z_i; \delta_{cell}) | j = 1, \dots, n_i)$. where (x_i, y, z_i) is the origin locations of synthetic cells, $((dx_j, dy_j) | j = 1, \dots, n_i)$ is the spatial offsets for the Gaussians, and δ_{cell} is standard deviation. We summarized all n_i of Gaussian intensity distribution and adjusted the integrated intensity to match I_{cell} for creating synthetic cells. This process is repeated for $I = 1, \dots, N$. We then multiplied the synthetic cells by adjusting green to red ratio of β and created those green synthetic cells. Finally, we acquired the synthetic cells in the fluorescent cryo-images with known locations.

6. Effect of k and *MIPD threshold* values on the algorithm performance

We investigated the effect of k (in k nearest neighbors) and the *MIPD threshold* on the algorithm performance. We would like to determine what should be the optimal values of these parameters so that the algorithm could be able to mostly clean the autofluorescence and minimally affect the detection of cells of interest. In this study, we created synthetic data by uniformly distributing 7,500 synthetic cells into two control livers. The number of 7,500 was estimated using the mean number of cell signals in the real liver datasets. We then repeatedly applied the cell detection and the cleaning algorithm to these synthetic datasets with different values of k and *MIPD threshold*. We varied the values of k from 1 to 50 and *MIPD thresholds* from 1 to 50. We measured the resulting errors in terms of *normalized errors* which were calculated using the sum of false positive rates and false negative rates. In this study, false positive rate = $FP/(FP+TN)$ and false negative rates = $FN/(FN+TP)$. The optimal k and *MIPD threshold* values should result in a minimal *normalized error*.

7. Algorithm testing using synthetic data

Our proposed algorithm was assessed for efficiently detecting green fluorescently labeled cells by sensitivity and specificity. In this study, we supposed that fluorescently labeled cells in the liver tend to be isolated whereas autofluorescent signals, which are mostly from the biliary tract, tend to be clustered in 3D volumetric data. From the hypothesis, we expected that our developed algorithm could be able to eliminate autofluorescent signals and maintain the cell signals of interest. To test the hypothesis, we added the created synthetic cells to the control cryo-images of the liver with no fluorescently labeled cells and applied an autofluorescent cleaning algorithm to these cryo-images. In this experiment, we had two representative control livers. We added 2,500, 5,000, 7,500, ... up to 20,000 synthetic cells into these two livers. We applied cell detection and autofluorescent cleaning algorithms to these datasets. We performed the 3D rendering (surface rendering) on the remaining cells to visually evaluate the cleaning performance. We also measured the number of detected voxels before and after the autofluorescent cleaning process. Since we knew the locations of the synthetic cells. The cell signals that are detected and unavailable in the list of the synthetic cells will be counted as false

positives. On the other hand, the cell signals that are not detected and available in the list of the synthetic cells will be counted as false negatives. The cell signals that are both detected and available in the list of the synthetic cells will be counted as true positives. In this study, Sensitivity = $TP/(TP+FN)$ and Specificity = $TN/(TN+FP)$.

8. Algorithm testing using real data

We applied our algorithm to real data. We had five different livers with green fluorescently labeled cells (real data). We applied the same cell detection and the cleaning algorithm to these five liver datasets. We then measured the number of detected voxels in pre-cleaning stage and post-cleaning stage to measure the cleaning performance. We performed the 3D rendering (surface rendering) on the remaining cells to visually evaluate the cleaning performance.

9. Workstation

In this study, we used Matlab 2021a (MathWorks) for developing and testing our proposed algorithm. We used Amira (Thermo Fisher Scientific) for visualizing fluorescent cryo-images and all the results in 3D volumetric data. The workstation consists of Intel® Core™ i7 CPU 975 @ 3.33GHz, 32.0 GB RAM, 64-bit operating system, x64-based processor under Windows 10 operating system.

ลิขสิทธิ์มหาวิทยาลัยเชียงใหม่
Copyright© by Chiang Mai University
All rights reserved

Chapter 4

Results and Discussion

The green cell detection algorithm could sensitively detect green cell signals as well as autofluorescent signals. We tested the algorithm using both livers with the real cell signals and livers with the synthetic cells. Three-dimensional visualization of the detected cell signals in Figure 4.1 showed that the cell signals appeared mostly as isolated points in liver tissues (Figure 4.1). Autofluorescent signals were also detected. When rendered in 3D, they mostly form noticeable structures (Figure 4.1). The structural noises were mostly from bile ducts, gall bladder, and connective tissues. These noises were the autofluorescent light released from biological structures within the biliary, tract and liver connective tissues.

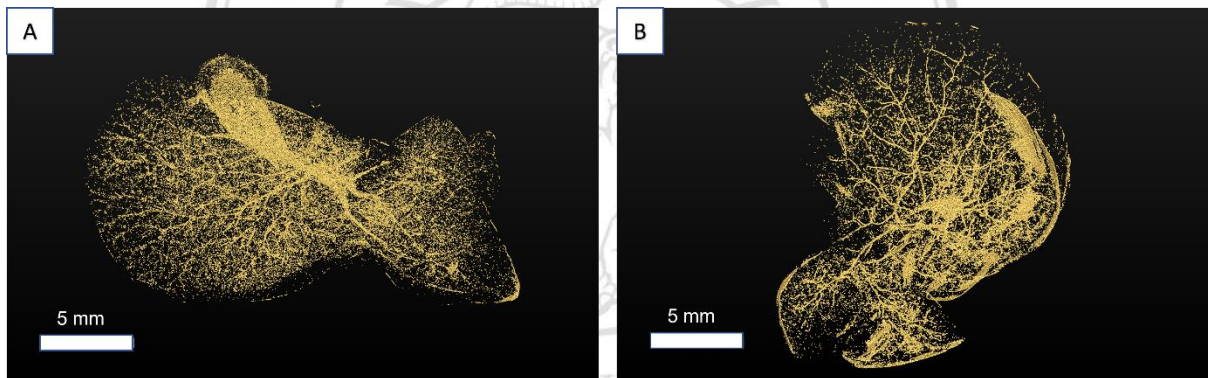


Figure 4.1 Surface rendering of the results generated by the green cell detection algorithm. The liver with green cells signals is in (A). The liver with synthetic cells is in (B). Cell signals of interest appeared as uniformly distributed isolated points while the autofluorescent signals appeared as structures.

We determined the effect of the parameters k and *MIPD threshold* on the autofluorescent cleaning performance. We used synthetic data for optimizing the parameters. To do so, we uniformly distributed 7,500 synthetic cells into two different control livers. The number was estimated by manually examining cell signals in the real data, which was around 5,000 – 10,000 cells per liver. We then applied the autofluorescent cleaning algorithm with different values of k and *MIPD threshold* as described in the Method chapter. We measured the numbers of cell detections, false positives, and false

negatives for each variation. The *normalized error* was calculated by sum of false positive rates and false negative rates. The relationship between the normalized error and the parameters, k , and *MIPD threshold*, is color-coded where red points represent higher error and blue points represent lower error. The result shows that the optimal k is in the range of [1, 5] while the optimal *MIPD threshold* is in the range of [5, 20]. The optimal values for eliminating autofluorescent signals with less impact on the cell detection are in the dark blue zone (Figure 4.2). In this study, we chose the k and *MIPD threshold* to be 3 and 15, respectively, for control liver 1 and we also chose k and *MIPD* to be 3 and 13, respectively, for control liver 2.

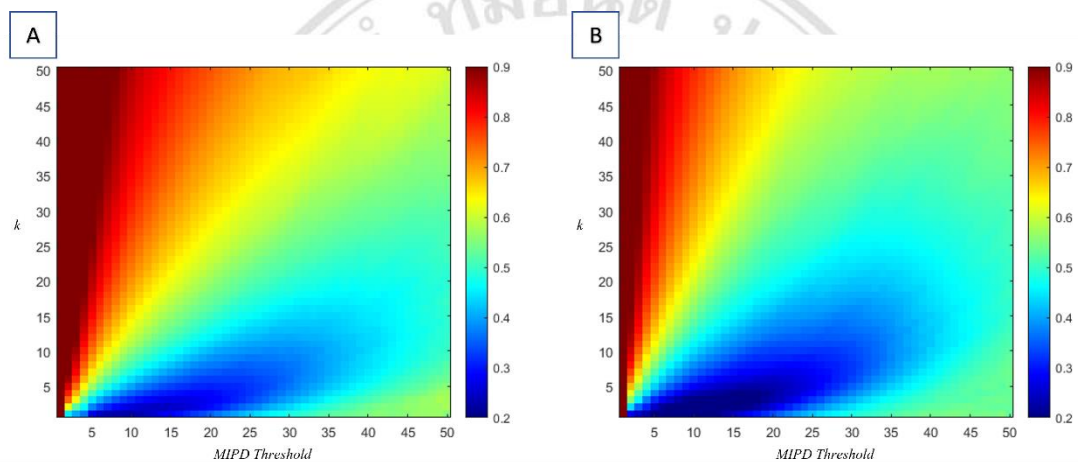


Figure 4.2 shows the relationship between the *normalized error*, and the parameters, k values from 1 to 50, and *MIPD* thresholds from 1 to 50 for control liver 1(A), and control liver 2(B).

We successfully cleaned the autofluorescent signals in control livers with synthetic cells. After optimizing the parameters, we applied the algorithm to the synthetic data created previously. The results of cell detections are shown in Figures 4.3A and 4.3C, for control liver 1 and control liver 2, respectively. After we applied the autofluorescent cleaning, the structured noises were mostly eliminated while the cell signals were mostly preserved, as shown in figure 4.3B and 4.3D.

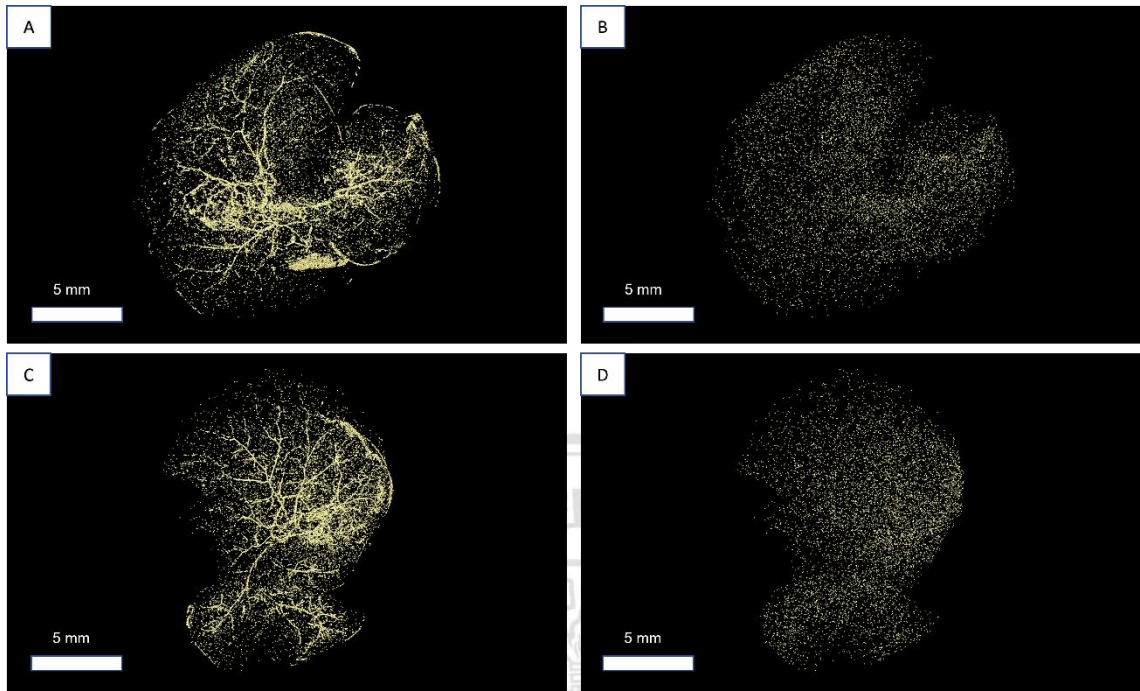


Figure 4.3 shows the image analysis of liver cryo-images with synthetic cells. The results of pre-cleaning consist of both cells of interest and autofluorescence (A, C) and post-cleaning show the eliminating of autofluorescence and maintaining of the cell of interest (B, D).

We conducted an additional experiment to test the robustness of the algorithm by adding different amounts of synthetic cells to the control livers. The number of detected voxels before the cleaning and after the cleaning, false positives, false negatives, sensitivity, and specificity for the control liver 1 were measured for the different number of added cells. Since we knew the exact locations of synthetic cells, we could count the number of false positives and false negatives from the list of synthetic cell locations. False positives were the number of detected voxels that the algorithm could detect but were not found in the synthetic cell list. False negatives were the number of detected voxels that the algorithm could not detect but were found in the synthetic cell list. The results were shown in Table I. The same analyses were applied to the control liver 2. The results were shown in Table II. The results showed that when we added more synthetic cells to the liver, the number of false negatives proportionally increased, while the number of false positives slightly decreased. We believed that by adding more cells into the liver, the detection per unit volume would increase. This subsequently rendered the cell detection in the liver to behave closely to the autofluorescence, which could result in a greater number of false negatives. Sensitivity was the proportion of true positives or synthetic

cells that the algorithm could detect. Specificity was the proportion of true negatives or autofluorescent noises that the algorithm could reject. Thus, the sensitivity values decreased from 87% to 80% in control liver 1 and 93% to 90% in control liver 2 (Figure 4.4A, Table I-II). By the same token, all autofluorescent noises were progressively eliminated as we added more cells. The specificity values were approximately 98% in both control liver 1 and control liver 2 (Figure 4.4B, Table I-II). Note that we used the same detection/cleaning parameters to all synthetic data.

Table I. Algorithm performance in control liver 1.

Control liver 1	Number of detected voxels (Pre-cleaning)	Number of detected voxels (Post-cleaning)	Number of false positives	Number of false negatives	Specificity	Sensitivity
2,500 cells	103,069	3,607	1,330	315	98.67	87.40
5,000 cells	105,301	5,644	1,277	616	98.72	87.32
7,500 cells	107,825	7,930	1,235	975	98.76	87.00
10,000 cells	110,375	10,159	1,177	1,485	98.82	85.15
12,500 cells	112,558	11,925	1,128	1,909	98.87	84.72
15,000 cells	114,799	13,672	1,100	2,539	98.89	83.07
17,500 cells	117,035	15,345	1,062	3,213	98.93	81.64
20,000 cells	119,273	17,058	1,071	3,904	98.92	80.48

Table II. Algorithm performance in control liver 2.

Control liver 2	Number of detected voxels (Pre-cleaning)	Number of detected voxels (Post-cleaning)	Number of false positives	Number of false negatives	Specificity	Sensitivity
2,500 cells	70,823	3,415	1,089	151	98.40	93.96
5,000 cells	73,278	5,720	1,045	290	98.46	94.20
7,500 cells	75,943	8,201	1,025	451	98.50	93.98
10,000 cells	78,212	10,277	987	622	98.55	93.38
12,500 cells	80,670	12,561	981	819	98.56	93.44
15,000 cells	83,237	14,864	967	1,102	98.58	92.65
17,500 cells	85,786	17,000	950	1,499	98.61	91.43
20,000 cells	88,359	19,085	943	2,000	98.62	90.00

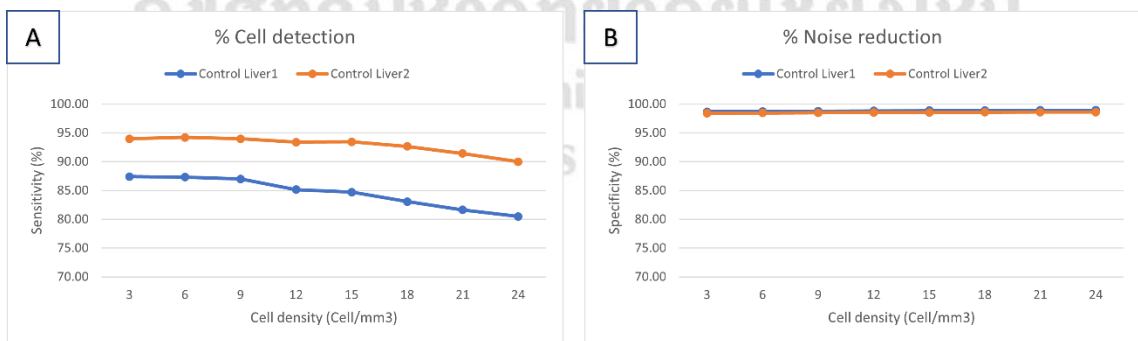


Figure 4.4 shows the relationship between Sensitivity and Cell density (A), and Specificity and Cell density (B).

We observed that an increasing number of false negatives or lost synthetic cells occurred when they were distributed close to the autofluorescence as shown in figure 4.6. Since our cleaning algorithm calculated the autofluorescence with density methods, we found that the more added synthetic increased their density in the liver volume and tended to be close to the autofluorescence.

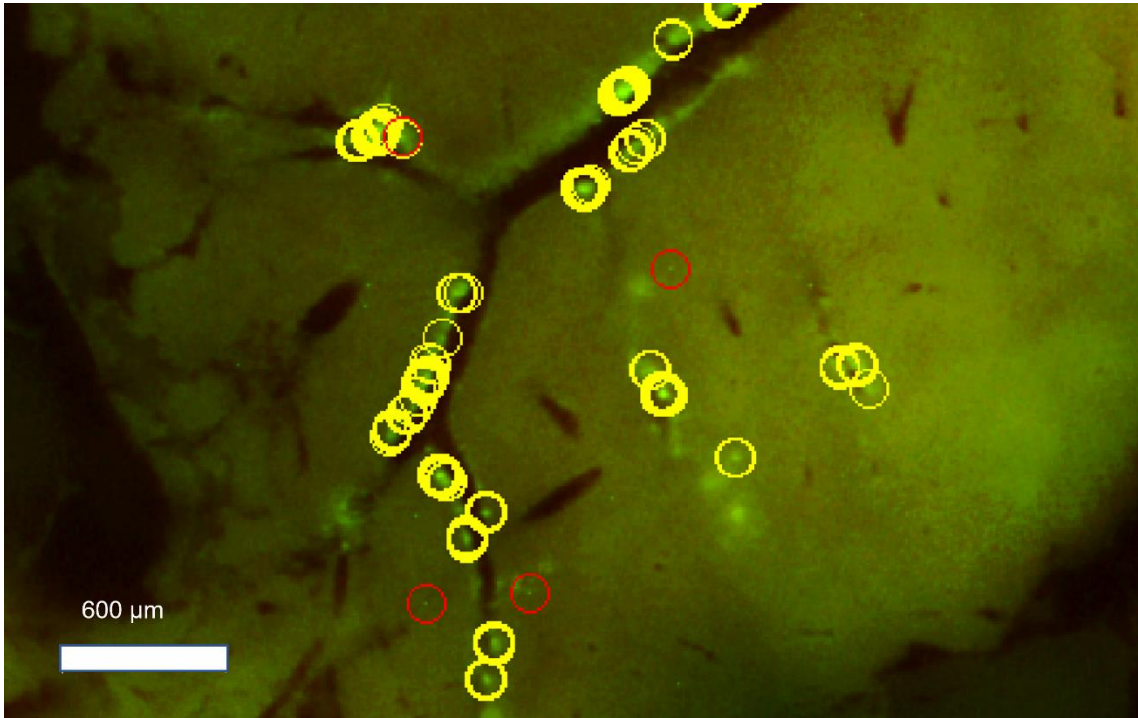
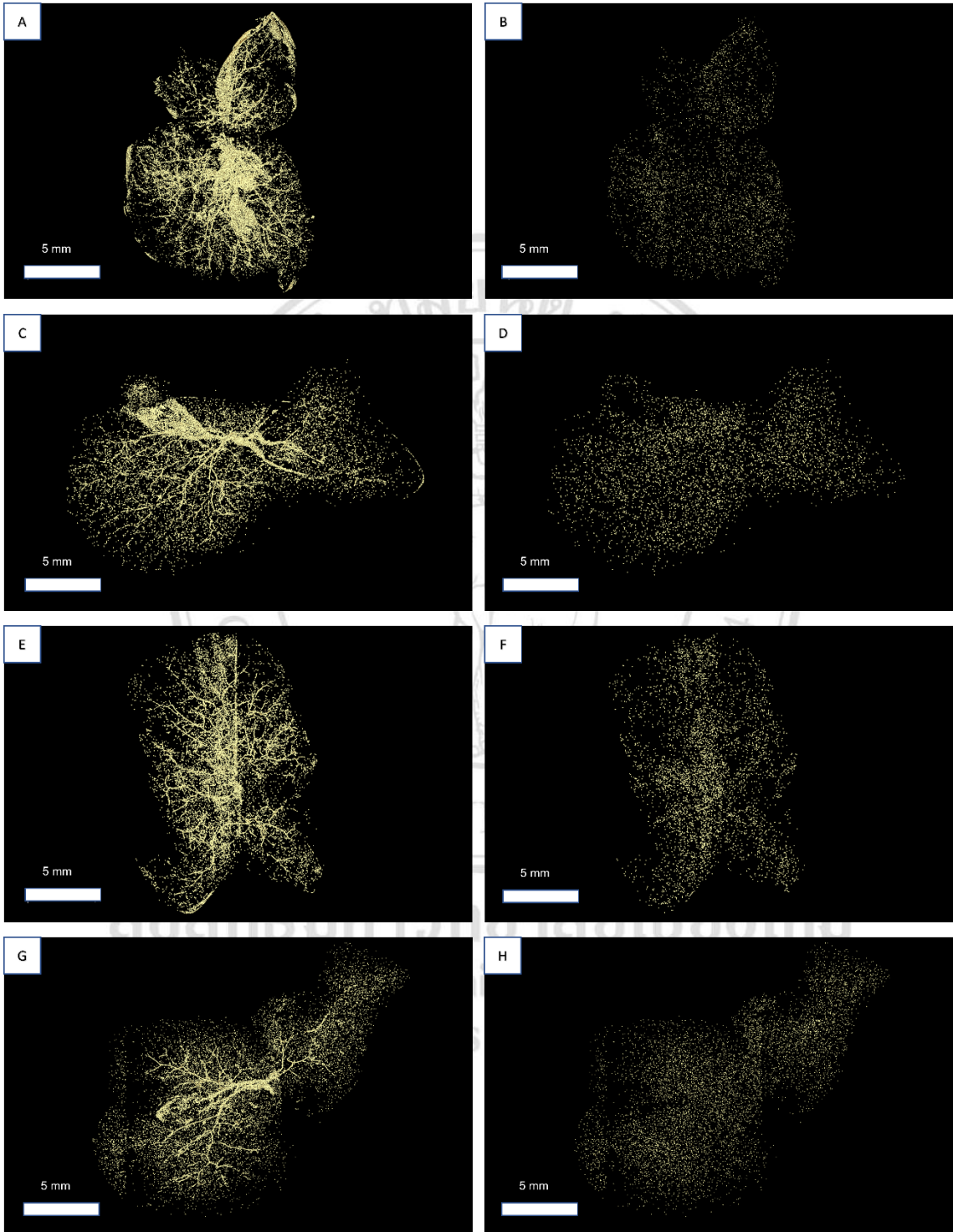


Figure 4.5 the red circles showed the false negative results or the synthetic cells that were wrongly removed and the yellow circles showed the autofluorescent noises that were correctly removed after the cleaning process.

The algorithm successfully detected the cells of interest and cleaned the autofluorescent signals in the livers with real cell signals. In this experiment, we used 5 representative livers with real cells from the mouse experiment. We observed that the algorithm was able to detect cell signals as well as eliminate most of the structural autofluorescent signals (Figure 4.6). Since we lacked the ground truth that indicated the actual locations of all cells in liver data, we manually examined the remaining cell detections to check if they were real cells or noises. The detections could be marked as the real cells if the detected blobs appeared only in the green channel but not in the red channel. We repeatedly checked the results and confirmed that 80-90% of the detections were probably the real cells, whereas the rest were the unstructured autofluorescence.



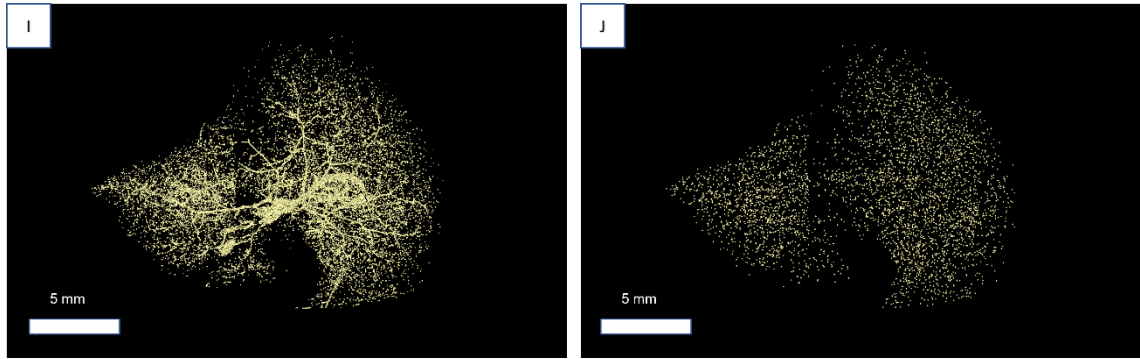


Figure 4.6 shows the image analysis of five different liver cryo-images with green fluorescently labeled cells. The results of pre-cleaning consist of cell signals and autofluorescence (A, C, E, G, I) and post-cleaning show the eliminating of structured autofluorescence and remaining of cell signals and unstructured autofluorescence (B, D, F, H, J).

We then performed quantitative analysis after applying the autofluorescent cleaning to the liver data with real cell signals. We measured the number of detected voxels before and after the cleaning using five representative livers. The first livers (Liver 1, Figure 4.6A) contained high autofluorescent density whereas the other four livers contained much lower autofluorescent density (Liver 2-5, Figure 4.6C, 4.6E, 4.6G, 4.6I). We observed that there are large autofluorescence structures in the first livers. Although the numbers of autofluorescent signals were reduced due to Mexican hat filtering and top-hat transformation with thresholding rules, the first liver still had remarkably high autofluorescence. By applying the cleaning algorithm to Liver 1, the number of detected voxels reduced from 263,131 to 4,885 which is a 98.14% reduction. We found that a large number reduction (98%) was due to the effectively structured noise-cleaning ability of the algorithm. The numbers are also reported in Table III. In addition, other livers with less autofluorescence (Liver 2-5) were also tested in the same way and yielded similar results (Table III). In Liver 4, we found that most of the detected voxels consisted of cell signals, thus the autofluorescent cleaning could reduce the number of detected voxels by around 87%.

Table III. The number of green fluorescently labeled cell detections. Liver 1 contains high noise density. Liver 2 - 5 contain low noise density.

	Number of detected voxels (Pre-cleaning)	Number of detected voxels (Post-cleaning)	%Detected voxels Reduction
Liver 1	263,131	4,885	98.14 %
Liver 2	112,275	5,459	95.14 %
Liver 3	84,941	5,435	93.60 %
Liver 4	83,335	10,711	87.15 %
Liver 5	87,451	4,731	94.59 %

The algorithm effectively eliminated structured autofluorescent signals in the liver data even if the liver had no cell signal. In this experiment, we applied the cleaning algorithm to liver data that had no fluorescently labeled cell or synthetic cell. The results showed that structured noises were effectively removed (Figure 4.7A, 4.7C). Only the unstructured noises remained. Interestingly, these isolated noises were distributed throughout the liver tissues. Therefore, our cleaning algorithm could not remove autofluorescent signals that looked like real isolated cells (Figure 4.7B, 4.7D). Further studies need to investigate the unstructured noises and we are still in need to develop an algorithm for cleaning these noises.

Copyright © by Chiang Mai University
All rights reserved

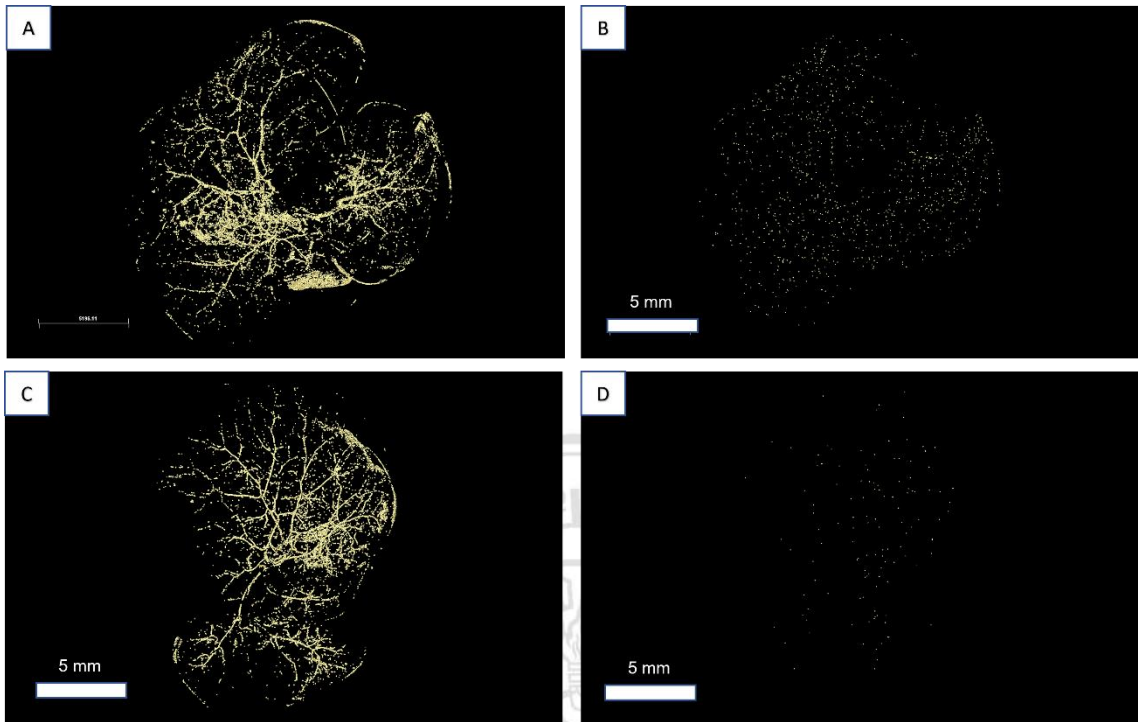


Figure 4.7 Results of applying the autofluorescent cleaning to the livers voided of cell signal. The results of pre-cleaning consist of only autofluorescence (A, C) and post-cleaning show the eliminating of structured autofluorescence and remaining of unstructured autofluorescence (B, D).

Chapter 5

Summary

We successfully developed an algorithm for detecting isolated green fluorescently labeled cells and cleaning autofluorescent signals in cryo-images of liver mouse samples for the first time. A challenge of this research was the detection of green fluorescently labeled cells among green autofluorescent noises, which are extremely difficult to distinguish. The key assumption for eliminating the autofluorescent noises was that voxels of the noises were assumed to be among a dense cluster of the voxels in 3D space. On the other hand, we assumed that the cell signals were isolated and distributed throughout the liver. We proposed that voxel density could be used to distinguish between the cells and the noises. We also proposed that the quantity to measure voxel density was a mean interparticle distance (MIPD) of the considering voxel to neighboring voxels. If the *MIPD* was less than a certain threshold, then the voxel of interest could be considered a noise because it was among a dense cluster. We suggested that the *MIPD* calculation could be performed efficiently using the *Kd-tree* data structure, where the searching complexity can be reduced from $O(n^2)$ to $O(n \log n)$.

We tested the algorithm performance using synthetic cells. The results show that the algorithm could effectively eliminate structural noises and had less impact on the detections of the green cells. The specificity values, that indicated the accuracy of the cell detection, were approximately 98%. (Figure 4.4B). However, the sensitivity values proportionally decreased from 93% to 80% as we added more cells from 2,500 to 20,000 (Figure 4.4A). We concluded that the cleaning capacity depended on cell density in the liver because most of the lost synthetic cells were distributed close to the autofluorescence (Figure 4.5).

We also tested the autofluorescent cleaning algorithm with the real data. Although we did not have ground truth indicating the actual location of all cells, we assumed that the quantitative results from the real data should be comparable with the ones from the synthetic data experiment. In the real data experiment, we applied the algorithm to 5 livers with real cells. The qualitative results showed that the structured autofluorescent noises were effectively removed (Figure 4.6). Our algorithm was considered successful in eliminating most of the structural autofluorescence signals that were mainly in the liver.

On the other hand, further studies of unstructured autofluorescent signals needed to be studied and developed in the future. Since we manually examined the remaining cells, we found that most of them were the actual T-cells. T-cells could be seen as the green spots against a greenish background in the fluorescent images because of the CFSE dyes (Figure 3.2). We observed that signals of the green cells (T-cells) appeared in the green channel but not in the red channel of the fluorescent image. In addition, we could also increase the magnification or use histology stains to verify that those green spots were the actual T-cells. We suggested that if we would like to study the details inside T-cells, we could use nucleus staining methods for identifying the features of the cells. However, the staining methods still had a limited field of view because of the very high magnification.

We realized that the aforementioned assumptions might not be valid in some situations. For example, if a mouse model had a chronic inflammation, T-cells would infiltrate potential lesions to neutralize foreign pathogens and perform healings [35]. Another example is that if a mouse model had T-cell priming in lymphoid tissues, the T-cells would highly be likely to form dense clusters [36]. In this study, we assumed that the mice used in this study had not yet developed any chronic inflammation or T-cell priming in the liver because the researchers injected the T-cells into the mouse only 24 hours before the imaging. We observed that most of the exogenous T-cells should either be in circulation or remained in an inactive state or mostly resided in the secondary lymphoid organs (such as spleen and lymph nodes). However, further biological experiments were needed to investigate all these confounding factors. Again, in this study, we were only interested in isolated T-cells in liver and ignored all clustered T-cells.

In conclusion, we developed an algorithm for detecting isolated green fluorescently labeled cells and eliminating largely structured autofluorescent signals for the first time. With our proposed algorithm, we could be able to solve the problem of autofluorescent interference and establish T-cell biodistribution. Since the T-cell distribution is established, we should be able to study the crucial role of T-cells that are particularly important in GVHD development. The limitation of our algorithm is specific only for the disease mouse model under cryo-imaging technology. Moreover, this study should expand the capability and biomedical applications of the cryo-imaging technology. Hopefully, we believe that the utilities of cryo-imaging technology will become more well-known and have a great impact on animal imaging research in the future.

References

- [1] H. Wang *et al.*, "Trafficking mesenchymal stem cell engraftment and differentiation in tumor-bearing mice by bioluminescence imaging," *Stem Cells*, vol. 27, no. 7, pp. 1548-58, Jul 2009.
- [2] T. Y. Liao, C. C. Liaw, K. H. Tsui, and Y. H. Juan, "Invasion of Adjacent Lumbar Vertebral Body from Renal Pelvis Carcinoma: Associated With Bone Metastasis But Easily Overlooked on Initial CT Scan," *In Vivo*, vol. 33, no. 3, pp. 939-943, May-Jun 2019.
- [3] E. J. Bernard SL, Barlow CH, Kelly JJ, McKinney S, Frazer DA, Glenn RW. High spatial resolution measurements of organ blood flow in small laboratory animals. *Am J Physiol Heart Circ Physiol*. 2000 Nov;279(5):H2043-52. doi: 10.1152/ajpheart.2000.279.5.H2043. PMID: 11045936., "Blery P, Pilet P, Bossche AV, Thery A, Guicheux J, Amouriq Y, Espitalier F, Mathieu N, Weiss P. Vascular imaging with contrast agent in hard and soft tissues using microcomputed-tomography. *J Microsc*. 2016 Apr;262(1):40-9. doi: 10.1111/jmi.12339. Epub 2015 Nov 2. PMID: 27002484.."
- [4] L. E. Jonkman, B. Kenkhuis, J. J. G. Geurts, and W. D. J. van de Berg, "Post-Mortem MRI and Histopathology in Neurologic Disease: A Translational Approach," *Neurosci Bull*, vol. 35, no. 2, pp. 229-243, Apr 2019.
- [5] R. Uppal and P. Caravan, "Targeted probes for cardiovascular MRI," *Future Med Chem*, vol. 2, no. 3, pp. 451-70, Mar 2010.
- [6] X. Wang, M. A. Jacobs, and L. Fayad, "Therapeutic response in musculoskeletal soft tissue sarcomas: evaluation by MRI," *NMR Biomed*, vol. 24, no. 6, pp. 750-63, Jul 2011.
- [7] S. J. Hectors *et al.*, "MRI radiomics features predict immuno-oncological characteristics of hepatocellular carcinoma," *Eur Radiol*, vol. 30, no. 7, pp. 3759-3769, Jul 2020.
- [8] D. Y. Lewis, D. Soloviev, and K. M. Brindle, "Imaging tumor metabolism using positron emission tomography," *Cancer J*, vol. 21, no. 2, pp. 129-36, Mar-Apr 2015.
- [9] H. Jadvar, "Molecular imaging of prostate cancer with PET," *J Nucl Med*, vol. 54, no. 10, pp. 1685-8, Oct 2013.

- [10] R. S. Driessen, P. G. Raijmakers, W. J. Stuijzand, and P. Knaapen, "Myocardial perfusion imaging with PET," *Int J Cardiovasc Imaging*, vol. 33, no. 7, pp. 1021-1031, Jul 2017.
- [11] Y. Li, W. Zhang, H. Wu, and G. Liu, "Advanced tracers in PET imaging of cardiovascular disease," *Biomed Res Int*, vol. 2014, p. 504532, 2014.
- [12] A. E. Gibbons, K. E. Luker, and G. D. Luker, "Dual Reporter Bioluminescence Imaging with NanoLuc and Firefly Luciferase," *Methods Mol Biol*, vol. 1790, pp. 41-50, 2018.
- [13] D. Desposito *et al.*, "Serial intravital imaging captures dynamic and functional endothelial remodeling with single-cell resolution," *JCI Insight*, vol. 6, no. 10, May 24 2021.
- [14] K. Toda, M. Tamamitsu, Y. Nagashima, R. Horisaki, and T. Ideguchi, "Molecular contrast on phase-contrast microscope," *Sci Rep*, vol. 9, no. 1, p. 9957, Jul 18 2019.
- [15] P. Wuttisarnwattana, M. Gargasha, W. van't Hof, K. R. Cooke, and D. L. Wilson, "Automatic Stem Cell Detection in Microscopic Whole Mouse Cryo-Imaging," *IEEE Trans Med Imaging*, vol. 35, no. 3, pp. 819-29, Mar 2016.
- [16] P. Wuttisarnwattana, S. Eid, M. Gargasha, K. R. Cooke, and D. L. Wilson, "Cryo-imaging of Stem Cell Biodistribution in Mouse Model of Graft-Versus-Host-Disease," *Ann Biomed Eng*, vol. 48, no. 6, pp. 1702-1711, Jun 2020.
- [17] P. Wuttisarnwattana, S. A. Raza, S. Eid, K. R. Cooke, and D. L. Wilson, "Novel T lymphocyte proliferation assessment using whole mouse cryo-imaging," in *SPIE Medical Imaging*, 2014, vol. 9038, p. 9: SPIE.
- [18] J. J. Auletta *et al.*, "Human mesenchymal stromal cells attenuate graft-versus-host disease and maintain graft-versus-leukemia activity following experimental allogeneic bone marrow transplantation," *Stem Cells*, vol. 33, no. 2, pp. 601-14, Feb 2015.
- [19] Z. Zhou *et al.*, "MRI detection of breast cancer micrometastases with a fibronectin-targeting contrast agent," *Nat Commun*, vol. 6, p. 7984, Aug 12 2015.
- [20] G. J. Steyer, F. Dong, L. Kanodia, D. Roy, M. Penn, and D. L. Wilson, "Detection and quantification of fluorescent cell clusters in cryo-imaging," *Int J Biomed Imaging*, vol. 2012, p. 698413, 2012.
- [21] M. Gargasha, M. Q. Qutaish, D. Roy, G. J. Steyer, M. Watanabe, and D. L. Wilson, "Visualization of color anatomy and molecular fluorescence in whole-

- mouse cryo-imaging," *Comput Med Imaging Graph*, vol. 35, no. 3, pp. 195-205, Apr 2011.
- [22] D. Roy, G. J. Steyer, M. Gargesha, M. E. Stone, and D. L. Wilson, "3D cryo-imaging: a very high-resolution view of the whole mouse," *Anat Rec (Hoboken)*, vol. 292, no. 3, pp. 342-51, Mar 2009.
- [23] D. Wilson, D. Roy, G. Steyer, M. Gargesha, M. Stone, and E. McKinley, "Whole Mouse Cryo-Imaging," *Proc SPIE Int Soc Opt Eng*, vol. 6916, pp. 69161I-69161I9, Jan 1 2008.
- [24] D. Roy, Case Western Reserve University]. OhioLINK Electronic Theses and Dissertations Center. http://rave.ohiolink.edu/etdc/view?acc_num=case1259006676.
- [25] P. Wuttisarnwattana, Case Western Reserve University]. OhioLINK Electronic Theses and Dissertations Center. http://rave.ohiolink.edu/etdc/view?acc_num=case1427978566.
- [26] Y. Ichiki, C. L. Bowlus, S. Shimoda, H. Ishibashi, J. M. Vierling, and M. E. Gershwin, "T cell immunity and graft-versus-host disease (GVHD)," *Autoimmun Rev*, vol. 5, no. 1, pp. 1-9, Jan 2006.
- [27] Prentice A. I. (1967). Autofluorescence of bone tissues. *Journal of clinical pathology*, 717–719. <https://doi.org/10.1136/jcp.20.5.717>.
- [28] S. Kretschmer *et al.*, "Autofluorescence multiphoton microscopy for visualization of tissue morphology and cellular dynamics in murine and human airways," *Lab Invest*, vol. 96, no. 8, pp. 918-31, Aug 2016.
- [29] S.-S. J. Larsen AK, Elvevold K, Ericzon BG, Mortensen KE, McCourt P, Smedsrød B, Sørensen KK. Autofluorescence in freshly isolated adult human liver sinusoidal cells. *Eur J Histochem*. 2021 Dec 13;65(4):3337. doi: 10.4081/ejh.2021.3337. PMID: 34897295; PMCID: PMC8696389.
- [30] S. T. Kotsiantis, George & Pintelas, P.. (2005). Bagging Model Trees for Classification Problems.. 328-337.
- [31] B. L. Eck *et al.*, "Comparison of quantitative myocardial perfusion imaging CT to fluorescent microsphere-based flow from high-resolution cryo-images," *Proc SPIE Int Soc Opt Eng*, vol. 9788, Feb-Mar 2016.
- [32] E. J. Bernard SL, Barlow CH, Kelly JJ, McKinney S, Frazer DA, Glenny RW. High spatial resolution measurements of organ blood flow in small laboratory

- animals. *Am J Physiol Heart Circ Physiol*. 2000 Nov;279(5):H2043-52. doi: 10.1152/ajpheart.2000.279.5.H2043. PMID: 11045936.
- [33] B. J. Quah and C. R. Parish, "The use of carboxyfluorescein diacetate succinimidyl ester (CFSE) to monitor lymphocyte proliferation," *J Vis Exp*, no. 44, Oct 12 2010.
- [34] J. B. Friedman, Jon & Finkel, Raphael. (1977). An Algorithm for Finding Best Matches in Logarithmic Expected Time. *ACM Trans. Math. Softw.* 3. 209-226. 10.1145/355744.355745.
- [35] K. Hirahara, A. Aoki, and T. Nakayama, "Pathogenic helper T cells," *Allergol Int*, vol. 70, no. 2, pp. 169-173, Apr 2021.
- [36] A. P. Benechet *et al.*, "Dynamics and genomic landscape of CD8(+) T cells undergoing hepatic priming," *Nature*, vol. 574, no. 7777, pp. 200-205, Oct 2019.



ลิขสิทธิ์มหาวิทยาลัยเชียงใหม่
Copyright© by Chiang Mai University
All rights reserved

CURRICULUM VITAE

Author's Name	Mr. Thanapong Chatboonward
Education	2016 Bachelor of Science in Associated Medical Sciences, Faculty of Associated Medical Sciences
Publication(s)	T. Chatboonward and P. Wuttisarnwattana, "Biliary Tract Autofluorescence Cleaning for Liver Cryo-imaging Data," <i>2021 18th International Conference on Electrical Engineering/Electronics, Computer, Telecommunications, and Information Technology (ECTI-CON)</i> , 2021, pp. 650-653, doi: 10.1109/ECTI-CON51831.2021.9454766.
Experiences	Medical Technologist at Sri Sang Wan Hospital, Mae Hong Son, Thailand



ลิขสิทธิ์มหาวิทยาลัยเชียงใหม่
Copyright© by Chiang Mai University
All rights reserved